



**Facultad
de
Ciencias**

**First-order correction of current
quantum capacitor models**

Corrección a primer orden de modelos de
condensador cuántico actuales

Trabajo de Fin de Grado
para acceder al

GRADO EN FÍSICA

Autor: Pablo González Mazón
Director: Javier Junquera Quintana

Junio 2019

Agradecimientos

La persona que más se merece el agradecimiento por este trabajo es el profesor Javier Junquera. Gracias por el buen trato que siempre he recibido de ti, y por haberte involucrado de la manera en que lo has hecho con este trabajo. También quiero dar gracias a los profesores de la Facultad de Ciencias por su gran labor docente, en especial a aquellos que me han ayudado este último año. Por su puesto, agradezco a todos mis amigos, dentro y fuera de clase, el seguir aguantándome.

Por último, doy gracias a mi padre y a mi madre por todo lo que hoy tengo, a mi hermano por haberme enseñado a pensar (aunque sigo haciéndolo peor que tú, yo soy más de imaginar) y a mi abuela, a quien dedico este trabajo. Gracias al resto de mi familia por cuidar de mí.

Abstract

In this work, a first-order correction of the capacitor models studied in the Physical Review B article [JGFS19] is proposed. The latter is a pioneer work in the incorporation of quantum effects to capacitance. In particular, it focuses on the contribution of the electrodes to the total capacitance. Although the analysis performed there is useful, the calculations are based on free electron models and are not yet susceptible to be incorporated into the construction of new devices. In this work, we try to extend the results of [JGFS19] to a more realistic system, which incorporates the atomic nature of matter. We propose a model in which the electrodes are simulated by 2D square, monoatomic lattices of Na. Using this model, we compute its capacitance and the most relevant contributions to it. Additionally, the similarity between our results and those obtained using free electron models is discussed, focusing on the theoretical description of the electron compressibility of the plates proposed in [JGFS19].

Key words: parallel-plate capacitor, capacitance, electron compressibility, SIESTA, tight-binding model, jellium

Resumen

En este trabajo se plantea una corrección a primer orden de los modelos de condensador que se estudian en el artículo de Physical Review B [JGFS19]. Este artículo es pionero en la incorporación de efectos cuánticos a la capacidad de condensadores. En particular, se centra en la contribución de los electrodos a la capacidad. Aunque el análisis realizado es útil, los cálculos están basados en modelos de electrones libres y aún no son susceptibles de incorporarse a la construcción de nuevos dispositivos. En este trabajo tratamos de extender los resultados de [JGFS19] a un sistema más realista, que incorpora la naturaleza atómica de la materia. Se propone un modelo en que los electrodos son simulados por redes cuadradas 2D de Na. Sobre éste, se calculan la capacidad y sus principales contribuciones. Adicionalmente, se discute la similitud entre los resultados obtenidos en los modelos de electrones libres y los aquí recogidos, haciendo especial énfasis en la descripción teórica de la compresibilidad electrónica descrita en ??.

Palabras clave: condensador de placas paralelas, capacidad, compresibilidad electrónica, SIESTA, modelo de enlace fuerte, jellium

Contents

1	Introduction	1
2	Negative capacitance	5
2.1	Foundations of capacitors	5
2.2	The idea of negative capacitance	7
2.3	Approaches to the origin of negative capacitance	9
3	Theoretical background	11
3.1	Equations governing the plate contribution to the capacitance	11
3.2	Previous results	16
3.2.1	Analytic calculations: 2D free electron gas	16
3.2.2	Numerical calculations: the electron confinement	17
4	The capacitance beyond free electron models	19
4.1	The general in-plane contribution	19
4.2	2D square, monoatomic Na layer	21
4.3	The capacitor model	21
5	Computational method	23
5.1	The tight-binding model	23
5.2	The SIESTA code	24
5.3	Numerical procedure	25
5.3.1	Electron compressibility, $d\mu/dn$	26
5.3.2	The perturbations $\Delta_{\text{H}}^{\text{right}}$ and Δ_{xc}	27
5.3.3	The image charge center z_{im}	27
6	Results	28
6.1	Derivation of the DOS within the tight-binding approach	28
6.2	Derivation of the in-plane contributions	30
6.3	Calculations for $a = 4.5\text{\AA}$	32
6.4	Calculations for $a = 6.8\text{\AA}$	38
7	Discussion	41
8	Conclusions	44
9	Appendix: the Python code	46

Chapter 1

Introduction

There is no doubt that the starring electronic component in the thriving of the electronic industry has been, since its discovery in the late 40s by Bardeen, Brattain, and Shockley at the Bell Laboratories, the transistor. Without them, the abysmal increase in the processing capabilities and miniaturization of modern devices, from smartphones to high-performance computers, would not have been possible. Surprisingly, despite their enormous possibilities, its functioning is quite simple to understand: they are switches that allow the circulation of current depending on the potential difference applied to one of the terminals. Furthermore, the amount of current that is allowed to cross them depends on the magnitude of this potential, enabling the modulation of the incident signal. The power of transistors lies in the fact that, when appropriately interconnected, they can simulate any logical operation.

It is natural to guess that the more transistors gathered inside a device, the more complex its response might be, as it can reproduce more logical operations. Therefore, from 1960 to 2010, new devices have been designed with progressively more transistors, and even to this date, it is yet one of the milestones of electronic industry (if something works well, why should we change it?). However, there are some impediments in the practical implementation of this idea. The first one has to do with the Joule effect and heat dissipation. Whenever the potential at some of the tiny switches changes, enabling or restricting the current flux (something that happens hundreds of times every second), there is a minuscule heat emission of the order of 10^{-16} J. Ignoring the energy losses attached to this process, if the density of transistors exceeds a critical value the dissipated heat can literally melt down the motherboard. As the emitted heat is proportional to the potential difference across the capacitor (Joule's law), the optimal performance demands the minimization of the potentials involved in the operation the transistor. To better understand how this can be achieved, we must look to another component integrated into every transistor: the capacitor. The function of the latter is to store an amount of charge that is proportional to the potential difference to which it is subject, according to a ratio that receives the name of capacitance. Thus, as large capacitances allow the manipulation of charge using low potentials, the enhancement of the capacitance is one of the objectives currently pursued by the microelectronics industry. To envision the different attitudes that have been adopted for such purpose, let us introduce the expression of the capacitance of typical parallel-plate capacitors

$$C = \frac{\kappa A}{4\pi d} . \tag{1.1}$$

Here κ is the dielectric constant of the interplate medium ($\kappa = 1$ for vacuum), and A , d are respectively the area and separation of the plates. In view of Eq.(1.1), one can think

of three possible methods to enhance capacitance: increase either κ or A , and reduce d . The value of κ depends on the nature of the material used as dielectric, and thus the first path requires either the research on the optimal materials for this purpose or the design and construction of new ones. The research on this direction, known as the “large- κ ” solution, is currently an opened line of investigation. However, it seems easier to simply modify geometric properties of the components such as A and d , and as miniaturization is also sought, the reduction of d happens to be the best choice. Indeed, this has been the typical solution adopted by producers: decreasing the size of capacitors would both lead to higher capacitances and leave more space for other components. Unfortunately, this is where the second problem arises. The rampant increase of the density of components in microprocessors that occurred since the 1960s led to the formulation of an empirical law by the engineer Gordon Moore, often known as Moore’s law [Moo98], which states that the number of transistors per unit of area doubles each year (later on, in 1975, the statement will be corrected to claim that the number of transistors duplicates every two years). The predicted exponential growth was supported by the processors developed within the hardware industry until 2016, when Intel postponed the release of its next generation of transistor technology and shut down the rule. The main reason why this technological trend has ground to a halt is that currents transistors, with sizes of the order of 10 nm, are approaching the quantum limit. This means that, in case of continuing reducing their size, quantum phenomena will become as relevant that the response of the material shall turn unpredictable. Namely, the electron currents due to tunnel effect increase exponentially as the interplate distance d diminishes, and it is no longer possible to keep on reducing this separation to get enhanced capacitors.

As quantum physics will eventually burst into the construction of microscopic capacitors, their study from the fundamental research perspective becomes necessary. In the last decades, several ways to further improve the capacitance of new components have been sought, some of them taking advantage of the quantum nature of matter. In order to get introduced to one of them, we recall some concepts from elementary electrostatics. It is well known that two capacitors connected in series have the same effect as a single capacitor with a capacitance given by the formula

$$C_{\text{tot}} = \left(\frac{1}{C_1} + \frac{1}{C_2} \right)^{-1}, \quad (1.2)$$

where C_1 and C_2 are the individual capacitances. We shall prove the latter expression in Chapter 2. However, according to Eq.(1.2) the overall capacitance will drop rather than increase, and hence this is not a favorable scenario. Nevertheless, we can infer what would happen in the case that one of the capacitors has a negative capacitance. If this is the case, Eq.(1.2) dictates that the capacitors connected in series are equivalent to a single one with a greater capacitance than the individuals. This idea steers to a new line of investigation: the so called negative capacitance. This modern field aims to design capacitors with improved properties, without further reduction of their size. Negative capacitance was firstly observed by Salahuddin and Datta in 2008, at the University of Purdue [SD08], who measured an amplification in the voltage at capacitors that contained ferroelectric materials under the presence of an alternating potential. This effect was ascribed to the rupture of the borders of ferroelectric domains in the sample materials due to the effect of the crystalline field of the surrounding atoms without a natural polarization, such as SrTiO₃. More recently, in 2016 Pavlo Zubko and his team [ZWH⁺16] found remarkable enhancements in the capacitance at superlattices constituted by alternating layers of ferroelectric atoms and others showing resistance to polarization. Again, this

discovery backed up the hypothesis of the displacement of ferroelectric domain borders as a cause of the negative capacitance. In view of the physical plausibility of this phenomena, the next step is to incorporate it to real capacitors. There are two possibilities: use materials showing negative capacitance either to the dielectric or to the electrodes. Rather than focusing on the optimization of dielectrics, which as in the case of the large- κ solution requires research in the design of new materials, in this work we shall study how negative capacitance affects the electrodes of the capacitor. To legitimize this choice, we must take into consideration that the stored charge remains almost entirely within these plates. Thus, the distribution of electrons is remarkably much more dynamic than in the interplate medium, and as we shall see, electrons play an important role in the definition of the total capacitance of a system.

In addition to the experimental support, an adequate theoretical framework is required to consider negative capacitance a valid physical theory. One of the pioneer works towards the mathematical foundations of the field was developed in 2009 by Thilo Kopp and Jochen Mannhart [KM09], who pointed to exchange-correlation interactions as the main responsables for the increase of capacitance, and deduced the equation that connects the total energy of a system with its capacitance. Also, they settled down some qualitative ideas that are necessary to get a complete understanding of negative capacitance from a theoretical perspective (we shall review their work in Chapter 2). Taking advantage of the recent theoretical advances, in 2019 Javier Junquera, Pablo García and Massimiliano Stengel [JGFS19] returned to the investigation about the origin of this effect. Namely, they made use of the Kopp-Mannhart equation to gauge the relevance of the different contributions of the energy functional to the total capacitance of a system, that modelled a parallel-plate capacitor. Although they used simple jellium slabs to obtain an approximation to the real underlying physics, new important effects that had remained unnoticed until their research were discovered. According to their calculations these new effects, of electrostatic nature, are the dominant source of the capacitance enhancements when the confinement of the electrons at the electrodes is low, and yet relevant in the strong-confinement regime. In view of their results, they questioned previous beliefs about the causes of negative capacitance, and pushed the exchange-correlation dominance into the background. Again, we will explain in detail the ideas of this paragraph in Chapter 2.

Despite the successes of the analysis carried out by J. Junquera, P. García and M. Stengel, its accuracy is strongly limited by the simplicity of the model. Indeed, one should not expect that a uniform background of positive charge, filled with free electrons, resembles the complex atomic nature of matter. Thus, a long research track is still required to achieve a complete understanding of the possibilities of negative capacitance, and how to include it in the design of microscopic capacitors. A possible next step towards this goal is to replace the unrealistic jellium model by an atomic lattice, repeating the same calculations in [JGFS19] to check whether its conclusions are right. There are two aspects to take into consideration before taking this step. First, it is foreseeable that the behavior of the capacitance in systems composed of atoms might be completely reliant on the chemical character of its atomic species and the crystalline structure of the lattice. Secondly, most of the typical materials of interest for solid state physics exhibit complex structures that are difficult to reproduce. A possible, yet simple, atomic approach to real systems are 2D crystals. Much of the theory developed within the context of negative capacitance (again, see [KM09]) is done for 2D electron gases, and they can resemble adequately the electrodes of a parallel-plate capacitor. Thus, 2D

systems are a good option to inspect whether the behavior of the negative capacitance studied in jellium systems show any significant variation with respect to atomic lattices.

This project aims to carry out a first-order correction for the jellium models discussed in [JGFS19]. We shall simulate a parallel-plate capacitor, where the electrodes are modelled using 2D-monoatomic layers of Na. Clearly, the latter is yet far from being a plausible approach to a real system. It is highly improbable for square monolayers to be used with such a purpose. Besides, very likely this structure for Na will not be stable, and it is not the best option for constructing electrodes neither. Rather than proposing a definitive model, this project targets a first inspection of the physics that discrete matter introduces in the study of negative capacitance. With this in mind, we propose the following two objectives: test the validity of the results obtained by Junquera, García, and Stengel; and continue with the long investigation track that is necessary to learn how to apply negative capacitance in practice, providing a first result background that can be used in future investigations. In connection to the second milestone, we aim to obtain results that go beyond the present project. We have already developed the software to repeat the same calculations as here using other atomic species and structures, meaning that we are in conditions to follow up with this research. However, for this project we have decided to limit to a simple case in which we have paid special attention, as we found more convenient to fully understand a basic scenario before giving the next step.

The content of this work is connected with many of the modules that are part of the bachelor degree in Physics arranged by the University of Cantabria. It is directly related to “Física Cuántica y Estructura de la Materia III: Física del Estado Sólido”, as our work has a deep relationship with free electrons and tight-binding models. Besides, we shall work with magnitudes such as densities of states, Fermi levels or electron compressibilities, which again lie on the field of solid state physics. While explaining the foundations of our model, we shall work with the electronic wavefunction of the electrons contained at the plates of capacitors. Furthermore, we will compute a perturbation over the Kohn-Sham Hamiltonian, meaning that we will also use techniques from quantum mechanics, studied in the module “Mecánica Cuántica”. Besides, as our goal is the understanding of capacitors, this work is also connected to basic electrostatics. Namely, we shall recall the description of the classical equation for the capacitance studied in “Electricidad y magnetismo”. Finally, this work is strongly reliant on computational calculations. Along its preparation, it has become necessary the design of multiple programs to carry out our study, and for the manipulation of the results. All the programs have been written in the PYTHON language. The developed software resembles the program designed in the module “Advanced Computation”, and many techniques learned from the subject have been employed here. In the Appendix, the constructed programs and methods are summarized.

Chapter 2

Negative capacitance

In this chapter, we review the ideas that led to the study of negative capacitance. We shall explain, using equations and qualitative ideas, the functioning of a capacitor as well as the expected behavior of a system showing negative capacitance. We will also derive some relevant expressions general for all capacitors, that will be particularly useful in our analysis.

2.1 Foundations of capacitors

A capacitor is an electronic device consisting of two confronted electrodes liable to freely charge, depending on the potential difference to which they are subject. Even though capacitors often have different geometries, they all can be understood from the analysis of the most basic example: the parallel-plate capacitor. In order to understand the shape of the electrostatic potential $V_H(z)$ along one of these capacitors, it is useful to recall the 1D Poisson equation

$$\frac{d^2 V_H(z)}{dz^2} = -\frac{4\pi}{\kappa} \rho(z) . \quad (2.1)$$

Here, κ is the dielectric constant of the interplate medium ($\kappa = 1$ for vacuum), and $\rho(z)$ is the charge density along the z direction. Assuming that the plates have an area A and are infinitely thin (i.e. we have a classical capacitor), the density ρ can be expressed as

$$\rho(z) = (Q\delta(z - z_1) - Q\delta(z - z_2))/A , \quad (2.2)$$

where Q/A is the areal density of charge, and z_1, z_2 are the positions of the plates in a reference system along the perpendicular direction to the plates. Hence, the integration of Eq.(2.1) leads to the following expressions for the electrostatic potential V_H and its derivative,

$$dV_H(z)/dz = \begin{cases} 0, & \text{if } z < z_1 \\ -\frac{4\pi Q}{A\kappa}, & \text{if } z_1 \leq z < z_2 \\ 0, & \text{if } z \geq z_2 \end{cases} \quad V(z) = \begin{cases} V_{\text{left}} & \text{if } z < z_1 \\ V_{\text{left}} - \frac{4\pi Q}{A\kappa}(z - z_1), & \text{if } z_1 \leq z < z_2 \\ V_{\text{right}}, & \text{if } z \geq z_2 \end{cases} ,$$

where we have chosen as the two boundary conditions for our second order differential equation

$$\begin{aligned} \frac{dV_H}{dz}(z = -\infty) &= 0 , \\ V_H(z = -\infty) &= V_{\text{left}} , \end{aligned}$$

and we have defined $V_{\text{right}} = V_{\text{left}} - 4\pi Q(z_2 - z_1)/A\kappa$. Hence, there is a discontinuity in the first derivative of the electrostatic potential at the positions of the plates, and whereas the potential remains constant outside of the plates, it decreases linearly along the interplate region.

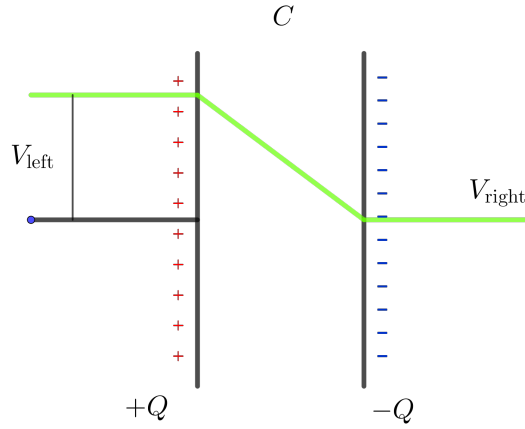


Figure 2.1: Schematic representation of a typical parallel-plate capacitor. Each plate has the same amount of net charge, with opposite signs. The electrostatic potential remains constant in the outer region of the plates, and shows a linear drop in the interplate region with a discontinuity of its first derivative at the plates.

Thus, the overall effect of the capacitor can be understood as a drop of the potential difference between its electrodes. The potential difference V at the terminals of a capacitor can be quantified in terms of the stored charge Q as the quotient

$$C = \frac{Q}{V} . \quad (2.3)$$

The ratio C is defined to be the capacitance of the system.

When two or more capacitors are connected in series, each one acts locally in the same way as the individual case. Remarkably, the net charge contained at every plate must, again, have the same magnitude. Indeed, the intermediate wires connecting two capacitors do not receive any extra charge, and must remain neutral. Thus, the charges “polarize” at the extremes of the wire, with opposite sign. Figure 2.2 depicts the electrostatic potential along a system with two capacitors connected in series. For the same reasons as before, the left and right capacitors produce a drop in the potential equal to V_1 and V_2 , respectively. Hence, the total potential difference equals the sum of the individual drops, $V = V_1 + V_2$. Using Eq.(2.3), the inverse of the total capacitance of the system can be computed as

$$\frac{1}{C_{\text{tot}}} = \frac{V}{Q} = \frac{V_1 + V_2}{Q} = \frac{V_1}{Q} + \frac{V_2}{Q} = \frac{1}{C_1} + \frac{1}{C_2} . \quad (2.4)$$

Therefore, two capacitors connected in series produce the same effect as a single capacitor with the total capacitance defined in Eq.(2.4). From the latter expression, it is straightforward that

$$C_{\text{tot}} = \left(\frac{1}{C_1} + \frac{1}{C_2} \right)^{-1} = \frac{C_1 C_2}{C_1 + C_2} < \min\{C_1, C_2\} ,$$

and the total capacitance is smaller than the individual ones.

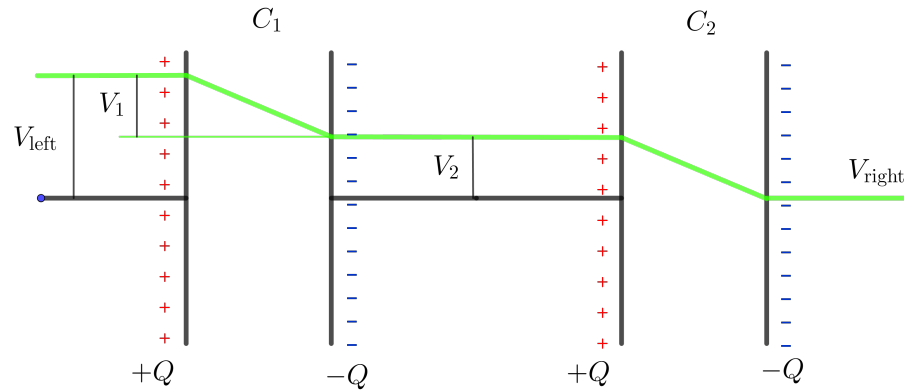


Figure 2.2: Schematic representation of two parallel-plate capacitors connected in series. Each plate has the same amount of net charge, with opposite signs at each capacitor. The drop in the potential is greater than in the single capacitor case.

2.2 The idea of negative capacitance

At first sight, it seems that there is no benefit in connecting two or more capacitors in series rather than using them separately, as we have explained that for industrial purposes higher capacitances are preferred. Albeit, the situation is different if one of the capacitors contributes with a negative capacitance. In Figure 2.3, the same scenario as in Figure 2.2 is represented, with the exception that the left capacitor is considered to have a negative capacitance.

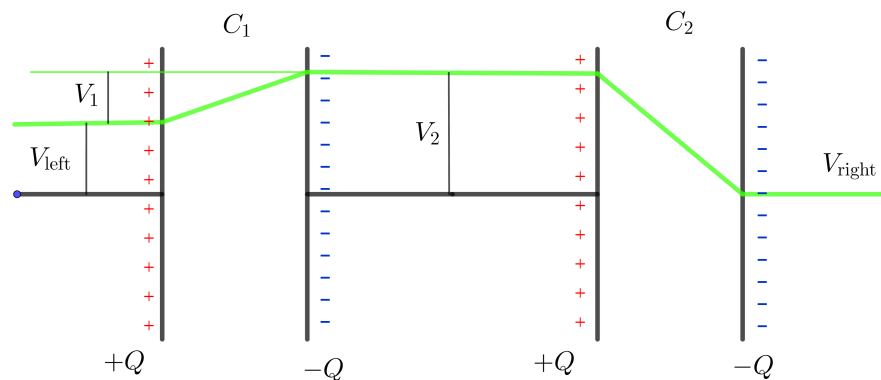


Figure 2.3: Schematic representation of two parallel-plate capacitors connected in series, when the left one has a negative capacitance (i.e. $C_1 < 0$). The drop in the potential is lower than in the single capacitor case, due to the effect of the negative capacitor.

In this situation, the left capacitor leads to a rise of the electrostatic potential. Indeed, according to Eq.(2.3) the sign of the potential must change, and the drop is inverted. Conversely, the overall variation in the potential is smaller than the individual effect of the right capacitor, and thus, the total capacitance is enhanced.

In order to design devices capable to work under the effect of very low potential differences it would be, therefore, incredibly useful to construct capacitors with a negative capacitance. This seems, a priori, impossible: a system with a negative capacitance must be necessarily thermodynamically unstable. To better understand the

previous assertion, it is useful to make use of the following relationship between the energy and the total capacitance of a system [FSL63]

$$\frac{1}{C} = \frac{d^2 E_{\text{tot}}}{dQ^2}(Q = 0) . \quad (2.5)$$

The latter equation can be understood as follows: the capacitance of a system coincides with the second derivative of its total energy with respect to the charge at the plates, when evaluated for neutral plates. We now proceed to deduce the above formula. The energy variation of a capacitor due to a differential variation of the charge at one of the plates can be expressed as

$$dE = VdQ = \frac{QdQ}{C} , \quad (2.6)$$

where Eq.(2.3) has been used for the second equality. Assuming that the capacitance remains constant, Eq.(2.6) can be integrated to obtain the total energy of the system

$$E = \frac{Q^2}{2} \frac{1}{C} . \quad (2.7)$$

Additionally, the total energy functional E_{tot} can be expanded to second order as a function of Q ,

$$E_{\text{tot}}(Q) = E_{\text{tot}}(0) + Q \frac{dE_{\text{tot}}}{dQ}(0) + \frac{Q^2}{2} \frac{d^2 E_{\text{tot}}}{dQ^2}(0) + \dots \quad (2.8)$$

When both electrodes remain neutral there is not energy stored at the capacitor, and $E_{\text{tot}}(0) = 0$. Furthermore, the total energy E_{tot} must be even with respect to the charge, as taking a charge Q from one electrode to the other is to all effects equivalent as taking $-Q$ from the second to the first (indeed, both plates are equivalent). Hence, it is straightforward that $dE_{\text{tot}}/dQ = 0$. Dismissing all the terms of higher order than two, Eq.(2.8) can thus be written as

$$E_{\text{tot}}(Q) = \frac{Q^2}{2} \frac{d^2 E_{\text{tot}}}{dQ^2}(0) . \quad (2.9)$$

The Eqs.(2.7) and (2.9) show a quadratic dependence of the energy with respect to the charge difference between the plates. Hence, identifying the energies at both equations, we have Eq.(2.5).

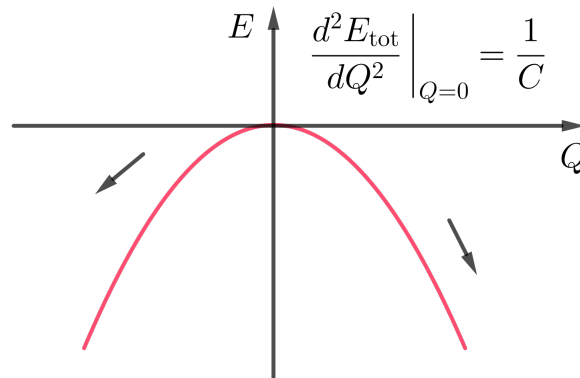


Figure 2.4: A system in a state where the energy shows a negative curvature is in an unstable equilibrium. It will evolve spontaneously to a lower energy configuration.

The reason for the instability of a capacitor with a negative capacitance is now clearer: according to Eq.(2.5), if the capacitance of a system is negative, the curve $E_{\text{tot}}(Q)$ is concave at the charge Q . Thus, the system will evolve spontaneously to a lower energy configuration (following the minimum energy principle) by either charging or discharging. It is important to highlight that negative capacitance is just a theoretical construction, as there is not physical sense for such systems that remain in an unstable equilibrium. We stress here that, if we connected in series a capacitor with negative capacitance to others with positive capacitance, as in Figure 2.3, then the equivalent capacitor would have yet a positive capacitance. Thus, there would be no thermodynamic impediment for the system.

2.3 Approaches to the origin of negative capacitance

Taking a step back, Eq.(2.5) is crucial in our context, as it provides a first way to study the capacitance of a system at the quantum level. Indeed, every contribution to the energy can thus be understood as a contribution to capacitance, and will be identified with a virtual capacitor. This conception, introduced by T. Kopp and J. Mannhart in [KM09], is the underlying idea of negative capacitance, and it is a key point to understand the equations that will be introduced in the following chapter. For our purpose, we can split the total energy functional as

$$E_{\text{tot}} = E_{\text{H}} + E_{\text{kin}} + E_{\text{xc}} + E_{\text{ext}} , \quad (2.10)$$

according respectively to the Hartree energy (E_{H}), kinetic E_{kin} and exchange-correlation (E_{xc}) energies of the electrons, and the energy variation produced by any other external contribution (E_{ext}). Figure 2.5 depicts a decomposition of a capacitor into four virtual parallel-plate capacitors connected in series, each of them according to one of terms in Eq. (2.10).

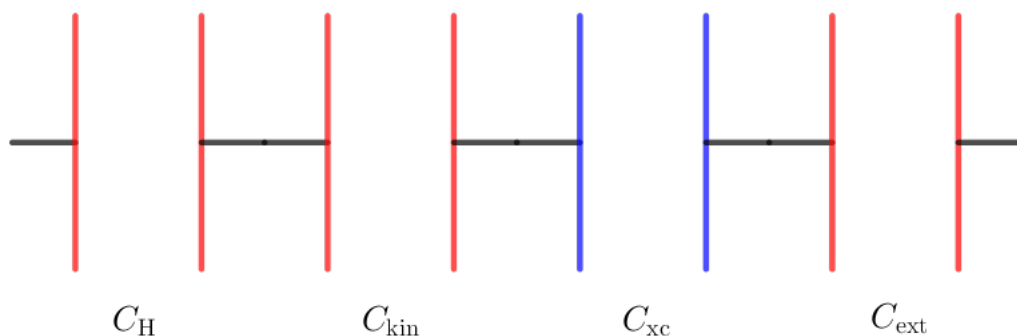


Figure 2.5: A capacitor can be decomposed into several “virtual” capacitors connected in series, each of them corresponding to one of the contributions to the total energy. The color indicates the sign the expected contributions to the total capacitance according to the expectations of T. Kopp and J. Mannhart: negative (blue) or positive (red).

As Figure 2.5 shows, Kopp and Mannhart pointed to the exchange and correlation energies as the origin of negative capacitance. For this conclusion they studied 2D systems of electrons checking that this was observed, and during years negative capacitance was ascribed to exchange-correlation effects in every system. However, a recent article from J. Junquera, P. García-Fernández and M. Stengel [JGFS19] have shed light over other effects of electrostatic nature that had remained concealed. Indeed, they found out that,

once the electrons are not restricted to a 2D plate, there is a displacement of the effective center of charge at the electrode. Consequently, the plate turns out to be equivalent to an “image” charge plane and the effective separation between the plates changes, leading to a variation of the total capacitance of the system. Thus, as the new effect has to do with the confinement of electrons, this makes one doubt about whether it is valid to extrapolate results calculated for a 2D confinement. The authors also realized that the electrostatic repulsion between the electrons entails a reduction in the exchange interactions, as well as a modification of the Hartree potential observed by both electrodes. For their conclusions, the authors of [JGFS19] focused their study on the contribution of the electrodes to the total capacitance of a simulated parallel-plate capacitor. To such purpose, they modelled these plates differently to get a broader physical view of the response of this system, but at all of them the positive charge was distributed as a uniform background, that receives the name of jellium.

An important simplification attached to jellium-like systems is that the electrons contained at the plates must be free. Even though the electrons in many real systems (for instance, alkali or noble metals) are well approximated by free electrons, it is foreseeable that some may localize at certain regions of a crystalline electrode. In consequence, it would be interesting to check whether the free electrons assumption is adequate for systems where the jellium background is dismissed, as it will give an idea of the applicability of all the results included in [JGFS19].

Chapter 3

Theoretical background

This chapter collects all the theory that backs up our calculations and analysis. We will employ the equations deduced in [KM09] and [JGFS19], as they constitute relevant part of the mathematical foundations that support the field of negative capacitance. Regarding that the analysis developed by Junquera, García and Stengel relied on the assumption of free electrons, in the present chapter we shall limit to free electron models.

3.1 Equations governing the plate contribution to the capacitance

In this section we introduce the equations that we will use in our calculations. The goal of this work is to define a procedure to compute the plate contribution to the capacitance of quantum capacitors, and to explicitly calculate the capacitance for a system that incorporates the atomic nature of matter. Hence, we are interested in formulas to describe all the different contributions to the total capacitance. The first equation that was introduced in this work, Eq.(1.1), was the classical expression of the capacitance for parallel-plate capacitors. In our analysis, it would be convenient to define the areal capacitance density $\mathcal{C} = C/A$ (as already mentioned, A denotes the area of the plates). From Eq.(2.3), it is straightforward that the classical equation for the inverse of the capacitance density is

$$\mathcal{C}_{\text{geo}}^{-1} = \frac{4\pi d}{\kappa}, \quad (3.1)$$

where the subindex “geo” indicates that this is a geometrical value (it depends exclusively on the interplate distance d). However, the last equation is nothing but a classical description, that disregards all the quantum effects we are interested in. There are two assumptions, inherent to classical electrodes, that are inadmissible to achieve an accurate description of the capacitance at the quantum level. The first one is the infinite density of states of the classical plates. This means that there are neither population restriction nor band structures. In a classical plate, all the electrons have the same energy. Secondly, the electrons inside a classical plate do not exhibit any spatial dispersion. Rather, they are constrained to a 2D region, and distribute homogeneously over the electrode. As we shall see shortly, these are relevant hindrances to achieve the description of capacitance we are looking for.

From now on, we will let n denote the electron number density at one of the plates of a capacitor, that is, $n = N/A$ where N is the total number of electrons contained

within an electrode of area A . Besides, in all the following we will use atomic units ($\hbar = e = a_0 = m_e = c = 1$).

A generalization for Eq.(3.1), that encompasses the quantum nature of matter, was firstly deduced in [JGFS19] from the Eq.(2.5) we deduced in Chapter 2. This equation is valid for systems where one of the electrodes is assumed to be classical. This might be, at first sight, an important restriction. However, the study of these kind of systems turns out to be equivalent to the study of real capacitors. Indeed, if a quantum electrode faces a classical one, the physics that it observes are the same as for a second quantum plate (we shall go over this idea again in the introduction of our capacitor model in Section 4.3). Hence, from now on we consider a parallel-plate capacitor where one of the electrode has a quantum nature and the second is classical. Without more interruption, the equation deduced in [JGFS19] is

$$C^{-1} = \frac{4\pi z_{\text{im}}}{\kappa} + \frac{d\mu}{dn}. \quad (3.2)$$

Here, $d\mu/dn$ is the electron compressibility of the quantum electrode, and z_{im} is the image charge separation between the electrodes. In the next pages, we shall explain in detail the meaning of each of these two terms.

First, we study the electron compressibility. For such purpose, we adopt the perspective of a 2D free electron gas, and consider a parallel-plate capacitor containing free electrons at each electrode. Although we aim to replace the free electron assumption for a more realistic physical model, the deductions here developed are valid for any other system (in Chapter 3 we shall explain how to generalize these formulas to more complex systems). If we choose the z direction to be orthogonal to the plates, we can assume that the electronic wavefunctions are the product of a wave plane along the plate direction, and an envelope function along the z axis

$$\psi_{\vec{k}_{\parallel}}(\vec{r}) = \psi(z) \cdot e^{i\vec{k}_{\parallel} \cdot \vec{r}}. \quad (3.3)$$

Thus, part of the the energy contribution to the system arises from a simple 2D free electron gas. Figure 3.1 represents a semi-filled energy band of a 2D free electron gas, together with its corresponding density of states (DOS).

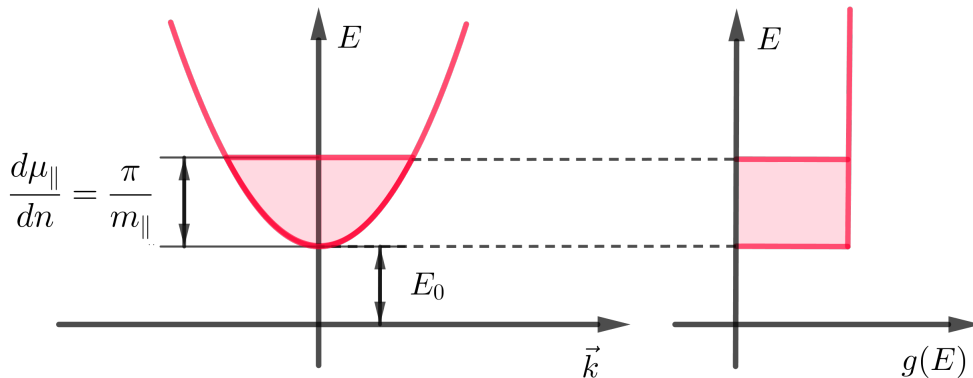


Figure 3.1: Schematic representation of a free-electron energy band, together with the corresponding density of states. The band follows a parabolic dispersion relationship:

$E_{\parallel}(\vec{k}_{\parallel}) = |\vec{k}_{\parallel}|^2/2m_{\parallel}$. The density of states for a 2D free electron gas, $g_{\text{FE}}^{2\text{D}}$, is a step function. The Fermi level of the system can be determined as a ground energy, E_0 , and the energy of the last populated state of the band.

The dispersion relation of the bands at a 2D free electron gas, as well as the corresponding density of states, are given by the following expressions

$$E_{\parallel}(\vec{k}_{\parallel}) = |\vec{k}_{\parallel}|^2/2m_{\parallel} , \quad (3.4)$$

$$g_{\text{FE}}^{2\text{D}}(E) = m_{\parallel}A/\pi , \quad (3.5)$$

where the \parallel subindex emphasizes that this energy contribution arises from the free electrons contained at the quantum electrode. The derivation of the total energy of such a system, which is entirely kinetic as the electrons are free, is an easy exercise. First, we find the following relationship between the electron population and the energy of the last occupied state

$$N = \int_0^{\mu_{\parallel}} g(\epsilon) d\epsilon = \frac{m_{\parallel}A}{\pi} \int_0^{\mu_{\parallel}} d\epsilon = \frac{m_{\parallel}A}{\pi} \mu_{\parallel},$$

$$\mu_{\parallel} = \frac{\pi n}{m_{\parallel}}. \quad (3.6)$$

The Fermi level of the free electron system can be expressed as a function of the electron density n , determined by the energy of the last populated state we have just deduced, and a ground energy E_0

$$\mu(n) = E_0 + \mu_{\parallel} = E_0 + \frac{\pi n}{m_{\parallel}}. \quad (3.7)$$

It is possible to derive the electron compressibility of this free electron system using Eq.(3.7). The electron compressibility is defined as $d\mu/dn$, and in our case, it can be decomposed as

$$\frac{d\mu}{dn} = \frac{dE_0}{dn} + \frac{d\mu_{\parallel}}{dn} = \frac{dE_0}{dn} + \frac{\pi}{m_{\parallel}}. \quad (3.8)$$

In view of Eq.(3.8), we find two different contributions to the electron compressibility. The first one is a constant in-plane contribution, that arises from the energy lift of the last occupied state, as the electron density n increases and more electrons populate the band. The second is the variation of the energy eigenvalue E_0 , which determines the energy of the ground state of the band, with respect to n . The latter contribution can be computed as

$$\frac{dE_0}{dn} = \frac{d}{dn} \langle \psi_0 | \hat{H} | \psi_0 \rangle , \quad (3.9)$$

where ψ_0 is the ground state wavefunction of the free electrons. We can use the Kohn-Sham hamiltonian to describe the energy of our system. This Hamiltonian is defined as

$$\hat{H} = \hat{T}_z + \hat{V}_H + \hat{V}_{\text{xc}} + \hat{V}_{\text{ext}} , \quad (3.10)$$

where \hat{T}_z is the component of the Kinetic operator in the z direction, and \hat{V}_H , \hat{V}_{xc} and \hat{V}_{ext} are respectively the Hartree, exchange-correlation and external potentials. However, the only operators that are dependent on the electron density n are the Hartree and the exchange-correlation potentials, \hat{V}_H and \hat{H}_{xc} respectively. Thus, using perturbation theory, it is possible to compute the variation of the eigenvalue of Eq.(3.9) as

$$\frac{dE_0}{dn} = \langle \psi_0 | \frac{d\hat{V}_H}{dn} + \frac{d\hat{V}_{\text{xc}}}{dn} | \psi_0 \rangle = \langle \psi_0 | \frac{d\hat{V}_H}{dn} | \psi_0 \rangle + \langle \psi_0 | \frac{d\hat{V}_{\text{xc}}}{dn} | \psi_0 \rangle . \quad (3.11)$$

In other words, it is possible to compute the variation of the energy eigenvalue as a perturbation of the Hamiltonian with respect to the electron density n . With this in mind, the electron compressibility can be rewritten as

$$\frac{d\mu}{dn} = \frac{\pi}{m_{\parallel}} + \Delta_{\text{H}} + \Delta_{\text{xc}} , \quad (3.12)$$

where the perturbative terms have been rewritten as

$$\Delta_{\text{H}} = \langle \psi_0 | \frac{d\hat{V}_{\text{H}}}{dn} | \psi_0 \rangle = \frac{1}{n} \int \frac{d\hat{V}_{\text{H}}}{dn} \cdot \rho(z) dz , \quad (3.13)$$

$$\Delta_{\text{xc}} = \langle \psi_0 | \frac{d\hat{V}_{\text{xc}}}{dn} | \psi_0 \rangle = \frac{1}{n} \int \frac{d\hat{V}_{\text{xc}}}{dn} \cdot \rho(z) dz , \quad (3.14)$$

and $\rho(z) = n|\psi_0|^2$ is the electron density function. We can further compact Eq.(3.12) including the perturbative terms as a unique one

$$\frac{d\mu}{dn} = \frac{\pi}{m_{\parallel}} + \Delta_{\text{tot}} . \quad (3.15)$$

Thus, there are two contributions to the electron compressibility: an in-plane term that arises from the variation of the energy of the last occupied state of the energy band, μ_{\parallel} , and a perturbation of the Hamiltonian along the z axis, with respect to the electron density at the plates. For technical reasons, the perturbation of the Hartree potential that must be computed for the application of Eq.(3.2) is $d(V_{\text{H}} - V_{\text{right}})/dn$ (see [JGFS19]), where V_{right} is the asymptotic value to which the Hartree potential tends for very large z (recall that we have seen that the electrostatic potential outside of the plates of classical parallel-plate capacitors is constant). Hence, rather than computing Δ_{H} , we shall calculate

$$\Delta_{\text{H}}^{\text{right}} = \langle \psi_0 | \frac{d(\hat{V}_{\text{H}} - V_{\text{right}})}{dn} | \psi_0 \rangle = \frac{1}{n} \int \frac{d(\hat{V}_{\text{H}} - V_{\text{right}})}{dn} \cdot \rho(z) dz . \quad (3.16)$$

Albeit, the equations explained here are yet valid for gaining the understanding of the underlying physics of the decomposition proposed in Eq.(3.15).

Now, we focus on the second contribution to the inverse capacitance density of Eq.(3.2). Recalling the electron density function $\rho(z)$ already defined, it is possible to compute the average charge center \bar{z} along the z axis as

$$\bar{z} = \frac{1}{n} \int dz z \rho(z) . \quad (3.17)$$

However, it is immediate to realize that $\rho(z)$ will vary as the electron density n changes (it must hold $\int \rho(z) dz = n$). Besides, it is reasonable to expect that the spatial distribution of the electrons must be distorted due to the attraction of the front plate, and as the overall system must remain neutral, this attraction will be stronger as the electron density at one of the plates increases, due to the charge difference between the plates. This distortion can be expressed in terms of the electron density function $\rho(z)$. Namely, we can define the image charge center as

$$z_{\text{im}} = \frac{d(n\bar{z})}{dn} . \quad (3.18)$$

The previous magnitude accounts for the variation of the average charge center with respect to the electron number density n . The reason why it is called the image charge center is that it is the “instantaneous” (at fixed n) center of charge of the electrode.

Ignoring the $d\mu/dn$ contribution, Eq.(3.18) coincides with the classical expression of the capacitance for classical parallel-plate capacitors, shown in Eq.(3.1), by just identifying

$d = z_{\text{im}}$. At fixed n , z_{im} represents the distance for which the action of one electrode is equivalent to that of a classical plate with the same net charge and located at z_{im} . In consequence, we can think on the capacitance of our system as that of a classical capacitor, where the separation between the plates is mobile. This opens, a priori, a new path for enhancing the capacitance. If the confinement of the electrons at the plates is not very strong, the displacement of the electronic cloud due to the potential difference will be notable. Hence, there will be a spontaneous reduction of the effective separation between the plates, which will lead, as discussed in the Introduction, to a enhancement of the capacitance. To envision this new phenomena, we include Figure 3.2, which illustrates the reduction of the effective interplate distance as a consequence of the image charge displacement.

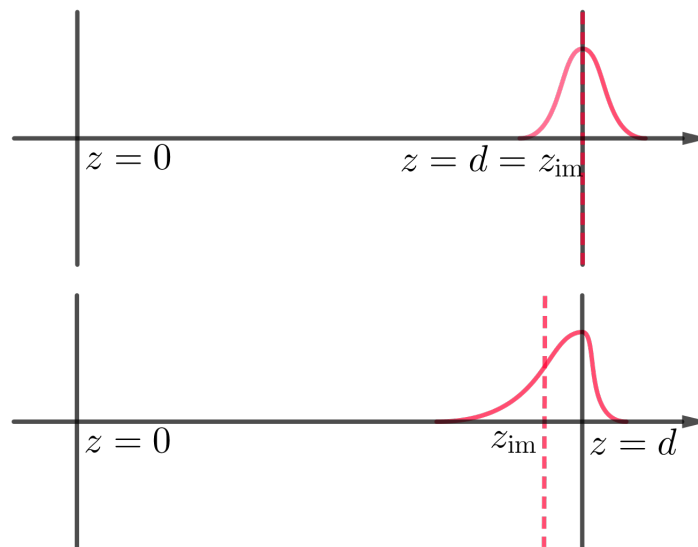


Figure 3.2: Displacement of the effective image charge center z_{im} of one electrode. The upper image represents the low n case, where the attraction of the front plate is not sufficiently large to distort the electron cloud, and this remains symmetrical around the plate. The lower image depicts a situation where n is sufficiently large for breaking the symmetry of the electron cloud, leading to a displacement of image charge center z_{im} . As the image shows, the displacement leads to a reduction of the effective interplate distance, and hence to an enhance of the capacitance.

The Eq.(3.2) is the generalization of Eq.(3.1) that we were looking for, as it encompasses the quantum nature of the electrodes. The new equation can be thought as the sum of a classical analogue contribution and a new purely quantum term: it is the sum of the capacitance of a classical parallel-plate capacitor with a “mobile” plate separation, and the electron compressibility.

We started this section explaining two shortcomings of the classical view against the quantum one: the infinitude of the density of states g and the neglecting of the spatial dispersion of the electrons. After having explained the contribution of the electron compressibility and the image charge center to capacitance, it is easier to understand why these two are important limitations. We finish this section explaining that Eq.(3.1) can be derived from (3.2).

Let us consider a classical plate. As in the previous paragraphs, we study first the $d\mu/dn$ contribution. The fact that in a classical electrode the DOS is infinite implies that, whenever a new electron is added to the plate, there are yet infinitely more states with the same energy available for the next one. Hence, the energy of the last occupied state is independent from the electron density n , and it must be $d\mu/dn = 0$. Following up with the image charge contribution, again the electrons are constraint to a 2D region, and the spreading along the z axis is not permitted. Thus $\bar{z} = d$ remains constant, and from Eq.(3.18) it follows that $z_{\text{im}} = d$. Finally, the expression of Eq.(3.1) is obtained.

3.2 Previous results

In order to compare our own calculations with previous results, in this section we review the conclusions of the pioneer work in [JGFS19], that studied the electrode contribution to the capacitance of a system. We first include the analytic expression for the inverse capacitance of a 2D free electrons gas. Later on, we discuss the analysis carried out in [JGFS19] for the different studied models.

3.2.1 Analytic calculations: 2D free electron gas

It is helpful, for the understanding of the results that we will expose in Chapter 6, to introduce the theoretical value of the inverse capacitance density when the plates are assumed to contain a 2D free electron gas. However, although this example is useful as a first contact with the inverse capacitance curve that we shall encounter, it is not a good model to compare our results with. The reason is that, in our results, the variation of the effective interplate distance as a consequence of the image charge center z_{im} displacement will be a crucial contribution to the system capacitance. The analytic equation that we include in the next paragraph is only valid for a 2D free electron gas, where the effective separation between the plates has a unique value d , independent of n . Thus, there is not possible charge center displacement, and one of the most relevant contributions is dismissed.

Regarding the expression of the exchange energy in the 2D limit, using a first order approximation of Eqs.(3.14),(3.16) to compute $\Delta_{\text{H}}^{\text{right}}$ and Δ_{xc} , and dismissing the effect of correlation (which is small in comparison with the other contributions), it can be derived (see [JGFS19], page 8) the following expression for the inverse capacitance density

$$\mathcal{C}^{-1} = \frac{4\pi d}{\kappa} + \left(\frac{\pi}{m_{\parallel}} - \frac{1}{\kappa} \sqrt{\frac{2}{\pi}} n^{-1/2} \right). \quad (3.19)$$

This equation provides a qualitative correct description of the growth of \mathcal{C}^{-1} , at least for the low n regime. As for this 2D electron gas $z_{\text{im}} = d$, we can identify $4\pi d/\kappa$ with the image charge term and $d\mu/dn$ with the quantity in brackets. The diverging term $\propto n^{-1/2}$ is due to the exchange interaction (indeed, here $\Delta_{\text{H}} = 0$ as the Hartree potential cannot change because the electrons are static, and neglecting the correlation it is possible to identify $\Delta_{\text{xc}} = -\frac{1}{\kappa} \sqrt{\frac{2}{\pi}} n^{-1/2}$). A graphical representation of the electron compressibility $d\mu/dn$, for a 2D free electron gas, is shown in Figure 3.3.

An equation similar to Eq.(3.19) can be generalized for the case of electrodes modelled by infinite and finite square wells, if the exchange interactions are modified using a form factor. However, we shall focus on numerical calculations over finite square well models, presented in the following section.

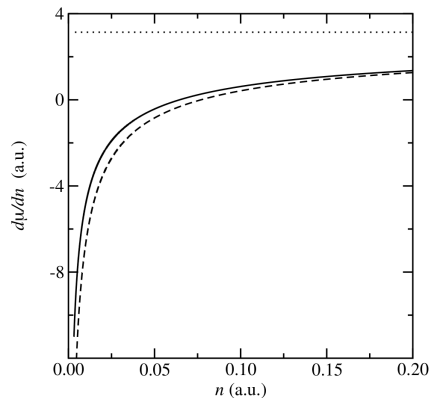


Figure 3.3: Electron compressibility of a 2D free electron gas, using Eq.(3.19) (solid line) and considering, in addition, the correlation contribution (dashed line). The contour of this curve coincides qualitatively with the inverse capacitance density \mathcal{C}^{-1} of all the free electron models that we shall analyze. Besides, we expect the same behavior in our calculations, at least for the low n regime.

3.2.2 Numerical calculations: the electron confinement

In the present section, we care about electron gases that have a finite thickness along the z direction. Namely, we shall focus on three different modellings for the electrodes: a traditional quantum well without inner positive charge, a traditional quantum well with an inner jellium background, and a jellium background without any confining potential. The study of these models is interesting for two reasons: first, as the electrons are no longer constrained to a 2D region, the displacement of the image charge center z_{im} is allowed; secondly, they include the effect of the electron confinement. The confinement will play an essential role in the final capacitance, as the distortion of the electron cloud will modify the evolution of \mathcal{C}^{-1} for large values of n , when the attraction between the electrons and the charged front plate is strong enough. Therefore, the inverse capacitance density shall depict a different behavior than the 2D case. Unfortunately, there is not an analytic equation neither for \mathcal{C}^{-1} nor $d\mu/dn$ in these examples. Hence, the calculations mainly consist on the numerical resolution of Eq.(3.2).

In the left plot of Figure 3.4 the value of \mathcal{C}^{-1} against the electron density n (red, solid line), together with $d\mu/dn$ (red, dashed line), are drawn for the case of the bare, square quantum well. The plot depicts a decline of \mathcal{C}^{-1} for sufficiently large electron densities, when compared with the 2D electron gas. This effect is produced by the reduction of the effective interplate distance, as z_{im} approaches the quantum electrode.

Evidently, the contribution of the image charge center is intimately dependant on the strength of the confinement. This is very well reflected in the comparison of the bare quantum well and the one filled with a uniform jellium background. Even though the presence of the well is an important limitation for the free displacement of z_{im} , the presence of the jellium at the latter adds an extra attraction that hinders the displacement of the image charge center. In order to envision the effect of confinement, in the right plot of Figure 3.4 we gather together the \mathcal{C}^{-1} curves for the three models introduced at the beginning of this section, and in Figure 3.5 we show the explicit variation of the image charge center. The inverse capacitance of the traditional well (red, solid line), illustrates a notable decline for large values of n , whereas the capacitance density of the well enclosing

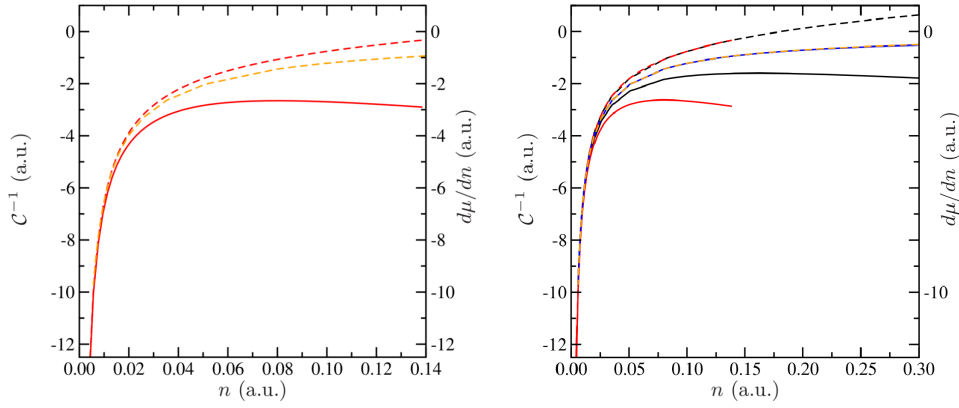
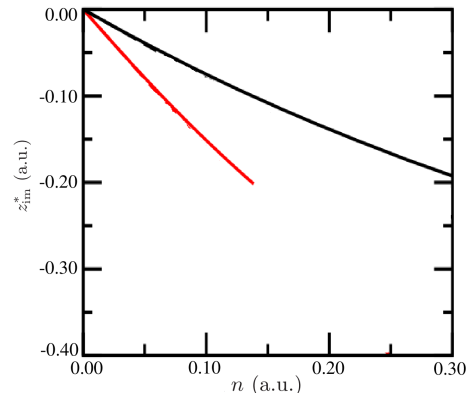


Figure 3.4: Left side: Inverse capacitance density of a parallel-plate capacitor (red, solid line) where the plates are modelled as finite, square wells. The data has been scaled to the geometrical value of \mathcal{C}^{-1} (i.e. the classical capacitance $\mathcal{C}_{\text{geo}} = \kappa/(4\pi d)$), and negative values for \mathcal{C} are permitted. The contribution of the electron compressibility is also plotted (red, dashed line). The orange curve represents the electron compressibility for the case where the electronic wavefunction is not allowed to distort, but we won't focus on this special case. Right side: Comparison of \mathcal{C}^{-1} (as solid lines), and $d\mu/dn$ (as dashed lines) at the finite square well with the jellium background (black) and without it (red). For large densities, the inverse capacitance at the jellium + square well mode is remarkably over the bare well case. The dashed blue-orange curve is, again, related to immobile wavefunctions, and we do not care about it.

the jellium positive charge shows a much more discrete reduction (the curve is almost constant) at the same n region. This coincides with what is observed in Figure 3.5, as the image charge center displaces remarkably more rapidly in the case of the bare well.

Figure 3.5: Variation of the effective charge center $z_{\text{im}}^* = z_{\text{im}} - d$ with respect to n , where d is the geometrical separation between the plates. The black lines correspond to the square well filled with a jellium, and the red lines to the well. As the confinement in the former is larger, the variation of z_{im} is more discrete.



Finally, if the confining square well is removed, leaving exclusively the jellium slab, the contribution of the image charge center becomes even more relevant. In the latter, the jellium is not able to hold the electrons at the surrounding of the quantum plate, leading to dramatic variations of z_{im} and consequent enhancements of the total capacitance (the new inverse capacitance is ~ 4 times lower than the square well cases).

Chapter 4

The capacitance beyond free electron models

Up to this point, we have exclusively cared about the study of the capacitance from the perspective of free electron models. Within this approximation, in Chapter 3 we have deduced an equation for the capacitance (Eq.(3.2)) that encompasses all the quantum phenomena we aim to include in order to get an accurate description of the electrode contribution to the capacitance of general capacitors. In the present chapter, try to generalize the analysis of 3 to a more global scope. Besides, we start our discussion of the atomic model that we shall employ in our calculations, as a correction for the free electron models already studied in [JGFS19]. Namely, we will model our electrodes as 2D square, monoatomic layers of Na. Even though this model is yet far from resembling the complex structures of real crystals used for the construction of electrodes, it is a good first step towards the industrialization of negative capacitance in device construction, as it incorporates the atomic nature of matter. To conclude the chapter, we introduce the specific model on which we perform our calculations.

4.1 The general in-plane contribution

In Figure 4.1, we define the objective of this work as a continuation of previous studies over free electron models. Once the plates are endowed with an atomic structure, the shape of the energy bands can vary enormously, always depending on the crystalline structure of the electrodes. Recalling the construction of Eqs.(3.5)-(3.8) of Chapter 3, we found that the variation of the energy of the last occupied state of the band with respect to the electron density, relative to the ground state of the band, $d\mu_{\parallel}/dn$, was one of the contributions to the electron compressibility. Namely, as the DOS for a 2D free electron gas is constant, we found that the corresponding contribution was also constant. Nevertheless, this is a very particular case, and in general the DOS is not constant. In particular, this is not the case of the 2D square crystals that we shall study.

The typical band structure for a 2D square lattice of *s*-like atomic orbital corresponds to the one displayed in Figure 4.1(c). As it is known from elementary solid state physics, as the atoms of a lattice approximate to each other the energy band “softens” at the limit of the Brillouin zone, leading to the the well-known cosine shapes. This fact transforms the associated density of states, as it entails the formation of a peak as shown in Figure 4.1(d). This is whatsoever contemplated in the theoretical equation for the compressibility that we deduced in Eq.(3.12). However, the equation for the capacitance can be generalized by

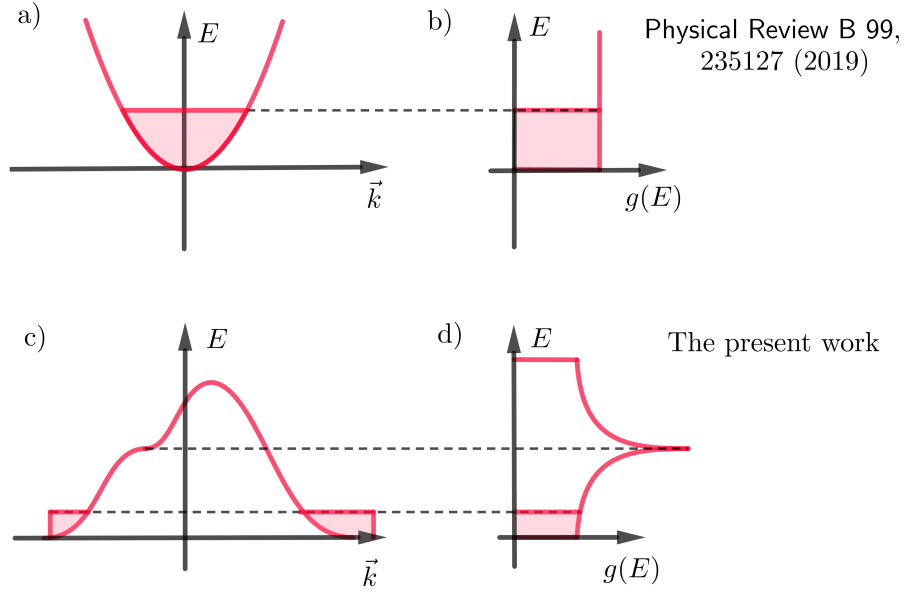


Figure 4.1: Comparison of the current state of investigation on the electrode contribution to the capacitance of quantum capacitors and the objective of this work. The upper images *a)* and *b)* illustrate, respectively, the energy bands and density of states of the free electron models that have already been studied in [JGFS19], and discussed in Chapter 3. In contrast, the images *c)* and *d)* depict the typical energy band and density of states formed for a 2D square lattice, that has not been studied until this work. As the lowest energy states of the atomic band can be well approximated by a parabola, at the beginning of the band population we expect the same behavior as in the free electron case. However, the rupture of the parabolic shape leads to new situations, as the divergence of the density of states. We want to shed light on how these phenomena affect the capacitance of a system.

just giving a step back. If the π/m_{\parallel} term is replaced by the variation of the energy of the last populated state of the band, μ_{\parallel} , a general equation for the capacitance can be written as

$$\frac{d\mu}{dn} = \frac{d\mu_{\parallel}}{dn} + \Delta_{\text{tot}} . \quad (4.1)$$

The $d\mu_{\parallel}/dn$ term is the in-plane contribution to the electron compressibility. All the other equations are completely valid for systems different to free electrons. Indeed, the perturbative contribution Δ_{tot} depends on the Hamiltonian, which is common to any system, and the image charge contribution is a classical analogue, again independent from the electron nature of the bonding formed at the electrodes.

In the nutshell, all the equations deduced in Chapter 3 are valid for general systems with the exception of the in-plane contribution. Therefore, the calculation of $d\mu_{\parallel}/dn$ becomes necessary to achieve an accurate description of the electron compressibility, and thus, for the capacitance. Nevertheless, the term μ_{\parallel} is intimately related to the density of states of the system. To tackle this issue, we shall compute the DOS from two different perspectives: first-principle calculations and the tight-binding model. The SIESTA software that we shall employ for all the calculations in this work provides the density of states of any simulated system. On the other hand, it is reasonable that the bonding formed in a 2D square,

monoatomic lattice resembles a tight-binding. We will compute the corresponding density of states within these two approaches, and derive the electron compressibility associated to each one. Obviously, we expect better results from the first-principle calculations of SIESTA, but it is also interesting to check the accuracy of the tight-binding in our system.

4.2 2D square, monoatomic Na layer

Since we are interested in comparing our results with those discussed in Chapter 3, coming from a model of free electrons, it is sensible to start choosing an alkali species for our square lattice. The reason for this choice is that the wave functions of the valence electrons coming from the s -shell spreads over many atomic distances, forming an electron-sea that can be very well approximated from the free-electron picture. Besides, an advantage of the 2D square, monoatomic lattice is that the density of states is very similar to that of a 2D free electron gas, g_{FE}^{2D} , at the borders of the band (i.e. when the band is almost empty or almost complete). Indeed, in these regions the DOS is locally planar, and we expect the same behavior as in the free electron case.

The tight-binding model that we shall study in the next section will exclusively consider the combination of s orbitals (we shall model the energy band using Eq.(5.3)). The case of Na is especially adequate for the comparison, as the assumption that the first band is composed entirely by the combination of s orbitals is reasonable. Nevertheless, this is not completely true, as in the real case there is always a small contribution of higher orbitals such as p or even d . We shall compare the bands that are formed for different lattice parameters in our lattice.

Another important point is to guarantee that we carry out our study using only a single band (the multiband case is remarkably more complex, and all the equations introduced at the beginning of Chapter 2 are developed within the single-band assumption, see [JGFS19]). Again, it is possible to modify the software specifications (SIESTA) to impose the formation of a unique band.

4.3 The capacitor model

Up to this point, we start explaining the framework of our analysis. All the calculations are made on the parallel-plate capacitor model introduced in Figure 4.2.

As we have anticipated in Section 3.1, we shall assume that one of the electrodes is “classical”. The reason why this assumption is valid is the fact that, in real capacitors, the electrodes are equivalent. Thus, for the study of the plate contribution to the capacitance of our model, we can limit our analysis to one of the electrodes. Besides, for most of our calculations we are interested in the cases where one of the plates has a deficit of electrons with respect to the other. This means that one of the electrodes is almost electronically bare. Hence, as the nuclear charges remain static (for the reasonable charge differences that we are interested in), no displacement of the effective center of charge is expected, and the classical assumption is completely valid.

Regarding the quantum plate, it is modelled as a 2D square, monoatomic lattice of Na atoms. In contrast to the classical plate, where all the charge is constrained to a 2D region (and hence the charge density at $z = 0$ is described by a $\delta(z)$), the spreading of the electron wavefunction (and consequently the electron density function $\rho(z)$) along the z axis is allowed. This fact is extremely important, as theoretical framework developed in

Chapter 3 lies partially on the “motion” of the electronic cloud contained at the quantum plate.

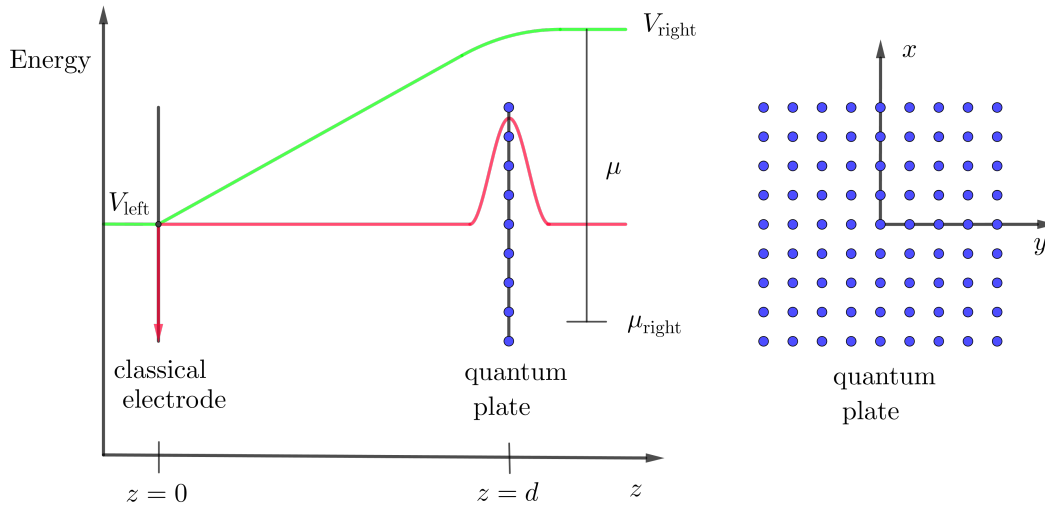


Figure 4.2: Left image: Scheme of the capacitor model. The classical electrode is located at $z = 0$ and the quantum plate at $z = d$. Although the latter is a 2D atomic layer, the spreading of the electron wavefunction (and thus the electron density function) in the z direction is allowed. The charge density is drawn as a red line, and the electrostatic potential as a green line (at $z = 0$ a δ function is pointing down because we have chosen inverted signs for the charge). For $z \leq 0$, $V(z) = V_{\text{left}}$ (there is a discontinuity in the derivative the potential at $z = 0$ due to the classical plate), and for large $z > d$ the potential tends asymptotically to a constant value V_{right} . Right image: orthogonal vision of the quantum plate, modelled as a 2D square monoatomic lattice.

For more simplicity in our description, the electronic charge is assumed to be positive. Thereby, the electrostatic energy and potential will numerically coincide, as the electron number density and the electronic charge density.

Chapter 5

Computational method

In this chapter, we are devoted to explaining the strategy followed for our calculations. We begin recalling the foundations of the tight-binding model that we shall use in our analysis, and in particular, we explain the chosen procedure for the computing of the density of states within this approximation, g_{TB} . Later on, we explain how to compute each of the magnitudes that will be required for the calculation of the electron compressibility and the image charge contribution to capacitance. Finally, we shall briefly review some elementary aspects of the SIESTA code that we shall use for our first-principle calculations, as well as other basics of the local density approximation theory.

5.1 The tight-binding model

The idea of the tight-binding model is to make linear combinations of individual atomic orbitals (LCAO), φ_μ , and to take advantage of the periodicity of the lattice, as every admissible wavefunction of the system must satisfy Bloch's theorem. An approximate wavefunction for a single electron in a crystal is

$$\psi_{m,\vec{k}}(\vec{r}) = \sum_{\mu} c_{\mu,m}(\vec{k}) \left[\frac{1}{\sqrt{N}} \sum_{\vec{R}_n} e^{i\vec{k}\cdot\vec{R}_n} \varphi_{\mu}(\vec{r} - \vec{R}_n) \right], \quad (5.1)$$

where N is the number of sites in the crystal, \vec{k} is the electron wavevector, φ_{μ} are atomic orbitals and \vec{R}_n are the centers of each φ_{μ} orbital (i.e. the core positions).

Although these wavefunctions are calculated as just an approximation, they can provide a good description of the electronic orbitals if the system is simple. Namely, they can be used to model a 2D monoatomic, square lattice. The accuracy of the tight-binding approach depends on the nature of the orbitals involved, as well as number of neighbors that each atom is considered to interact with. However, if the set of considered orbitals and neighbors is very large, the complexity of the calculation increases significantly. The description is enormously simplified if all the orbitals are chosen to be identical (for instance, s orbitals) and the first-neighbors assumption is adequate (i.e. the overlapping of the wavefunctions of distant atoms is neglected).

As we have already explained, the in-plane contribution requires the calculation of the density of states. Thus, we proceed to deduce the expression of the density of states for a 2D electron gas in the tight-binding context. The density of states associated to a 2D energy band can be calculated using the relation

$$g(E) = \int_{\text{BZ}} \frac{d\vec{k}}{(2\pi)^2} \delta(E - E_B(\vec{k})) , \quad (5.2)$$

where the subindex BZ indicated that the integral is extended to all the Brillouin zone. If the tight-binding approximation is limited to s orbitals with the interaction of exclusively the first neighbors (we shall check whether this assumption is reasonable in our case at Chapter 6), the energy of the first band of a square, monoatomic lattice is given by the expression (represented in Figure 5.1)

$$E_B(k_x, k_y) = \alpha + 2\gamma(\cos(k_x a) + \cos(k_y a)) , \quad (5.3)$$

where α is the overlap integral and γ is the interatomic hopping integral. According to the properties of Dirac deltas, the following equality holds

$$\delta(E - E_B(\vec{k})) = \sum_{E_B(\vec{k}_0)=E} \frac{1}{|\nabla E_B(\vec{k})|} \delta(\vec{k}_0 - \vec{k}) . \quad (5.4)$$

Using the previous equality, it is possible to rewrite Eq.(5.2) as

$$g_{\text{TB}}(E) = \frac{1}{(2\pi)^2} \int_{l=E_B^{-1}(E)} \frac{dl}{|\nabla E_B(l)|} , \quad (5.5)$$

where $l = E_B^{-1}(E)$ is the set of points contained in the Brillouin zone with exactly the energy E . Hence, the density of states at the energy E , $g(E)$, can be computed as the line integral over all the wavevectors at the Brillouin zone with the same energy E . After having computed the density of states, we can make use of the fundamental theorem of calculus to compute the variation in the electron compressibility associated to the in-plane energy of the electrons. Indeed, we have

$$n(\mu_{\parallel}) = \int_{-\infty}^{\mu_{\parallel}} g(E) dE = G(\mu) - G(-\infty) , \quad (5.6)$$

where G is a primitive function of g . Deriving with respect to μ_{\parallel} ,

$$\frac{dn}{d\mu_{\parallel}}(\mu_{\parallel}) = g(\mu_{\parallel}) \quad , \quad \frac{d\mu_{\parallel}}{dn}(n) = \frac{1}{g(\mu_{\parallel})} , \quad (5.7)$$

where we have used the inverse function theorem for the right equality.

5.2 The SIESTA code

All the first-principles calculations have been carried out using the software SIESTA [SAG⁺02], a package especially designed for electronic structure calculations in solids and molecules. The software allowed to simulate the system introduced in Figure 4.2,

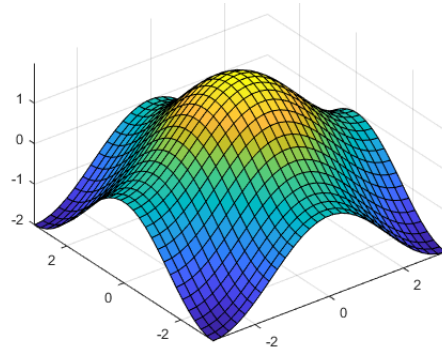


Figure 5.1: First energy band of a square, monoatomic lattice due to the combination of s orbitals (using first neighbors only). For the representation, $\alpha = 0$ and $\gamma = 0.5$ have been chosen. The lower axis represent the normalized wavevectors (k_x/a , k_y/a independently, the function is symmetric), and the z axis the energy.

enabling the choice of the atomic species for the quantum plate, the crystalline lattice and motif, the atomic separations and the interplate distance. With these ingredients, the software (and its analysis package MACROAVE) allowed the computation all the magnitudes mentioned above.

SIESTA solves the Schrödinger equation for the electrons in our system from first-principles, i.e. without any parameter taken from experiment. First-principles calculations are free from parameters, but they are not free from approximations. In particular:

1. The pseudopotential approximation to treat the interaction of the core-electrons and the nuclei on the valence electrons.
2. The local density approximation (LDA) within the density functional theory to deal with the difficult electron-electron interactions.
3. The use of a strictly localized basis set of numerical atomic orbitals to expand the eigenvalues of the Hamiltonian. Here, we have considered one s -orbital to deal with the $3s$ -shell of the Na atoms. But in order to reproduce the eventual deformation of the charge density as a response to the electric field generated by the classical electrode, we also included a shell of polarization p -orbitals. These orbitals are higher enough in energy to avoid the crossing of the majority p -band with the s -band.
4. The use of a regular finite grid in real space to compute the integrals between atomic orbitals.
5. The use of a regular finite grid in reciprocal space to sample the electrons in the first Brillouin zone.

5.3 Numerical procedure

For the calculations in this work, we have developed a specialized software. Its functioning can be summarized in the following steps:

1. **INPUT:** A set of equispaced lattice parameters $\{a_i\}_{i=0}^{N_a} = \{a_0 + i\delta a\}_{i=0}^{N_a}$ and electron densities $\{n_j\}_{j=0}^{N_n} = \{n_0 + j\delta n\}_{j=0}^{N_n}$. Every simulation will be determined by exactly a pair (a_i, n_j) of these magnitudes.
2. The program starts writing the text file where the output data will be allocated.
3. A double loop is started, running over all (a_i, n_j) pairs, $0 \leq i \leq N_a$ and $0 \leq j \leq N_n$. For each pair, the code modifies the input file of SIESTA, which outputs the Fermi level of the quantum plate $\mu_{\text{right}}(a_i, n_j)$, as well as the files containing the raw data of the Hartree potential $V_{\text{H}}(\vec{r})$, the electron density function $\rho(\vec{r})$ and the exchange-correlation potential $V_{\text{xc}}(\vec{r})$ for the pair (a_i, n_j) at every point in space \vec{r} .
4. Using the SIESTA extension MACROAVE, the files containing the unprocessed information of $V_{\text{H}}(\vec{r})$ are macroscopically averaged in order to obtain nanosmoothed values of the potential that depends only on the cartesian coordinate z , $V_{\text{H}}(z)$. The values of z form an equispaced set of points $\{z_0 + k\delta z\}_{k=0}^{N_z}$, that maps all the simulated cell. Only at this step (not at 5 or 6), the value $V_{\text{right}} = V_{\text{H}}(z_0 + 0.9N_z \cdot \delta z)$ is taken.
5. Step 4 for $V_{\text{xc}}(z)$.

6. Step 4 for $\rho(z)$.
7. Using the functions calculated at steps 4, 5, 6, we compute $d\rho/dn(z)$, $dV_{xc}/dn(z)$ and $d(V_H - V_{\text{right}})/dn(z)$. After these, we compute $d\mu/dn$, z_{im} , Δ_H^{right} and Δ_{xc} for the pair (a_i, n_j) .
8. Using Eq.(3.2) we compute the numerical value of \mathcal{C}^{-1} , and compare it with the same value computed using the theoretical equation (4.1).
9. **OUTPUT:** A text file containing $d\mu/dn$, z_{im} , $z_{\text{im}}^* = z_{\text{im}} - d$, \mathcal{C}^{-1} , $\mathcal{C}^{*-1} = \mathcal{C}^{-1} - 4\pi d/\kappa$, $\Delta_{\text{tot}} = \Delta_H^{\text{right}} + \Delta_{xc}$, for every value (a_i, n_j) .

Next, we explain in detail the calculation of all the relevant magnitudes listed before. These are: $d\mu/dn$, $d\rho/dn$, dV_{xc}/dn , $d(V_H - V_{\text{right}})/dn$, z_{im} , Δ_H^{right} , Δ_{xc} and \mathcal{C}^{-1} .

5.3.1 Electron compressibility, $d\mu/dn$

Recalling that $\mu = \mu_{\text{right}} - V_{\text{right}}$, where μ_{right} is the Fermi level of the right electrode, it is possible to compute it from the Fermi level and the Hartree potential. One of the key points of our software is the numerical calculation of $d\mu/dn$. For a fixed lattice parameter a , the code generates the complete list $\mu(n_j) = \mu(n_0 + j\delta n) = \mu_{\parallel}(n_0 + j\delta n) - V_{\text{right}}(n_0 + j\delta n)$. It is possible to compute $d\mu/dn$ applying finite differences,

$$\frac{d\mu}{dn}(n_j) \sim \frac{\mu(n_j + \delta n) - \mu(n_j - \delta n)}{2\delta n} = \frac{\mu(n_{j+1}) - \mu(n_{j-1})}{2\delta n}. \quad (5.8)$$

Obviously, the accuracy of the numerical derivative is directly related to the length of δn (and the smaller δn does not always imply an improvement of the calculation, as it can amplify errors). This method (centered finite differences) is repeated for all the numerical derivatives that are computed along this work.

On the other hand, in order to understand the origin of the electron compressibility, we are interested in comparing the numerical values of the compressibility, computed using Eq.(5.8), with those generated by Eq.(4.1). For such a purpose, the calculation of $\Delta_{\text{tot}} = \Delta_H^{\text{right}} + \Delta_{xc}$ becomes necessary, as well as the energy of the last populated state relative to the ground state of the band μ_{\parallel} . Recalling Figure 3.1, the perturbative term describes the variation of the eigenvalue of the Hamiltonian (i.e. the ground state of the band) with respect to n , and the in-plane contribution $d\mu_{\parallel}/dn$ describes variation of the energy of the last occupied energy state of the band relative to that eigenvalue, again with respect to n . To compute the in-plane contribution, we must first calculate the density of states g of our band. We shall compute this density of states within two different perspectives: the first-principle calculated DOS that SIESTA outputs, g_C , and the DOS computed within our tight-binding approach, g_{TB} . In the following, we maintain the notation g_C and g_{TB} to allude to each of the densities of states.

For the calculation of g_{TB} we make use of Eq.(5.5). The first step is the calculation of the equienergetic curves of the dispersion relation given by (5.3). Secondly, the line integral over each of these curves must be solved. A (local) parametrization for these equienergetic curves is given by

$$l(u) \equiv E_B^{-1}(u) = (u, \cos^{-1}((E - \alpha)/2\gamma - \cos u)), \quad u \in (-\epsilon, \epsilon) \quad (5.9)$$

for sufficiently small $\epsilon > 0$. The gradient of E_B is

$$\nabla E_B(k_x, k_y) = (-2\gamma a \sin(k_x a), -2\gamma a \sin(k_y a)).$$

As the function $|\nabla E_B(k_x, k_y)|$ has the same symmetry of a square (recall Figure 5.1), we can use the parametric representation of Eq.(5.9) to compute

$$g_{\text{TB}}(E) = 4 \int \frac{1}{\sqrt{1 - (e - \cos u)^2 + \sin^2 u}} \sqrt{1 - \frac{\sin^2 u}{(1 - (e - \cos u)^2)}} du, \quad (5.10)$$

where we have compactly written $e = (E - \alpha)/2\gamma$ and the integral is extended to one fourth of the equienergetic curve.

5.3.2 The perturbations $\Delta_{\text{H}}^{\text{right}}$ and Δ_{xc}

As we have just explained, the terms $\Delta_{\text{H}}^{\text{right}}$ and Δ_{xc} are required to compute the theoretical electron compressibility, according to Eq.(4.1). Taking advantage of the sets $\{V_{\text{H}}(z_k)\}_{k=0}^{N_z}$ and $\{V_{\text{xc}}(z_k)\}_{k=0}^{N_z}$ computed by MACROAVE (the set $\{z_k\}_{k=0}^{N_z}$ is a sampling of $2^{16} = 65536$ points), the followed strategy is to compute the functions dV_{xc}/dn , $d(V_{\text{H}} - V_{\text{right}})/dn$ as

$$\frac{d(V_{\text{H}} - V_{\text{right}})}{dn}(z, n_j) \sim \frac{(V_{\text{H}} - V_{\text{right}})(z, n_j + \delta n) - (V_{\text{H}} - V_{\text{right}})(z, n_j - \delta n)}{2\delta n}, \quad (5.11)$$

$$\frac{dV_{\text{xc}}}{dn}(z, n_j) \sim \frac{V_{\text{xc}}(z, n_j + \delta n) - V_{\text{xc}}(z, n_j - \delta n)}{2\delta n} = \frac{V_{\text{xc}}(z, n_{j+1}) - V_{\text{xc}}(z, n_{j-1})}{2\delta n}. \quad (5.12)$$

Using the sampling $\{\rho(z_k)\}_{k=0}^{N_z}$ and the trapezoid rule for integration, Δ_{tot} can be computed from Eqs.(3.14) and (3.16).

5.3.3 The image charge center z_{im}

For the calculation of z_{im} , the computation of the derivative of the charge density $\rho(z)$ function with respect to n is required, and the same exact strategy as in Eqs.(5.11) and (5.12) is followed

$$\frac{d\rho}{dn}(z, n_j) \sim \frac{\rho(z, n_j + \delta n) - \rho(z, n_j - \delta n)}{2\delta n} = \frac{\rho(z, n_{j+1}) - \rho(z, n_{j-1})}{2\delta n}. \quad (5.13)$$

It turns out that Eq.(3.18) is equivalent to

$$z_{\text{im}}(n) = \int dz z \frac{\rho_{\text{tot}}}{dn}(z, n), \quad (5.14)$$

and again, applying the trapezoid rule, we can integrate along the z direction using the sampling of the interval and the trapezoid rule. To conclude, from $d\mu/dn$ and z_{im} , the derivation of the inverse charge density \mathcal{C}^{-1} is straightforward.

Chapter 6

Results

In this chapter we include all our calculations, with comments and comparisons. Even though our main goal is the calculation of the inverse capacitance density C^{-1} of the system described in Figure 4.2, we are specially devoted to testing whether the decomposition of the electron compressibility given by Eq.(4.1) is further valid to the extent of our model. In addition to this, we are interested in the comparison of our results with those calculated using free electron models and jellium slabs, discussed in Section 3.2.

We begin this chapter introducing our calculation of the density of states within the tight-binding approximation, g_{TB} . After this, we follow up checking that, in view of the first-principle calculations of the electronic bands and density of states formed at the quantum plate, the electronic structure is likely to be approximated by a tight-binding. Later on, we present our calculations of in-plane contributions using both the g_{C} and g_{TB} densities of states. We finish developing a detailed analysis of our calculations of the electron compressibility, charge image center and inverse capacitance. To achieve a broader vision of the underlying physics of our model, we repeat all this process for the lattice parameters of $a = 4.5\text{\AA}$ and $a = 6.8\text{\AA}$, analyzing whether the same conclusions are extracted.

In all the calculations, we consider $\kappa = 1$. Besides, we limit our analysis to the study of the first energy band. As we have already explained, the studied band is exclusively formed by the combination of s orbitals. Each of these orbitals cannot host more than 2 electrons. Hence, we are only interested in those densities for which there are 2 electrons per atom at most. Thus, in all the chapter, we will sweep all the electron densities going from $n_{\text{min}} = 0$ to $n_{\text{max}} = 2/a^2$, where a is the lattice parameter of our 2D square, crystal.

6.1 Derivation of the DOS within the tight-binding approach

As we have already pointed out, in our tight binding approximation we consider exclusively the combination of s orbitals, and we restrict to first-neighbor interactions. With this assumptions, we can ensure that the energy of the band can be described by Eq.(5.3). In Figure 6.1, some equienergetic curves of this band contained, inside the Brillouin zone, are shown. According to Eq.(5.5), the number of available states for the energy E , $g_{\text{TB}}(E)$, is calculated as a line integral along the corresponding equienergetic curve.

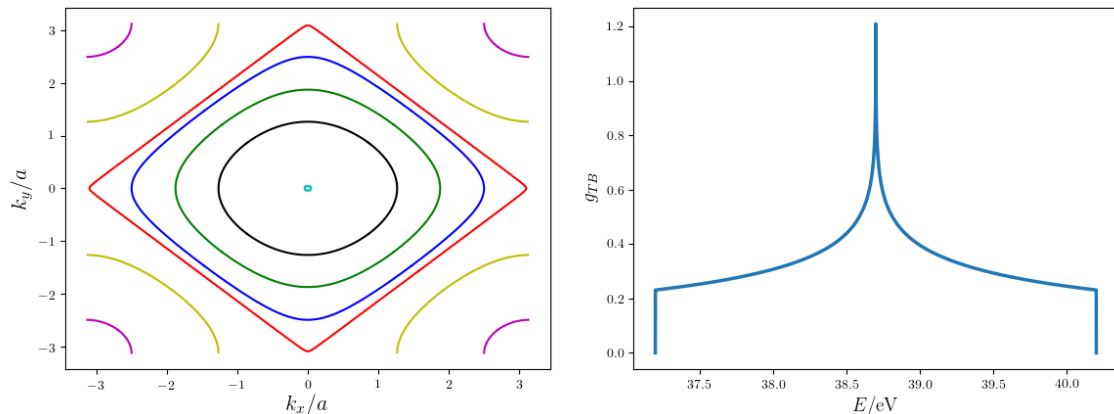


Figure 6.2: Left side: Brillouin zone the 2D square, lattice that composes the quantum plate. Some equienergetic curves for the band of Eq.(5.3) have been drawn. The corresponding $(E_B - \alpha)/2\gamma$ values are: -1.8 (magenta), -0.7 (gold), 0.01 (red), 0.2 (blue), 0.7 (green), 1.3 (black), 1.999 (cyan). Right side: Numerical calculation of the density of states, g_{TB} , for a 2D square lattice in the tight-binding approximation. The parameters $\alpha = 0$, $\gamma = 0.5$ have been chosen.

The computed density of states, g_{TB} , is shown in Figure 6.2. The most remarkable aspect of the curve is the presence of a pronounced peak at those states corresponding to the half-full band. This contrasts with the constant shape of the 2D free electrons case, g_{FE}^{2D} , given by Eq.(3.5). To better understand the divergence in the new contour, it is helpful to take a look to Figure 6.1. With $\alpha = 0$, the shape of curves becomes less soft as the energy approaches 0, leading to a square contour (if the surface of Figure 5.1 is intersected with the $E_B = 0$ plane, a square is obtained). Hence, the value $|\Delta E_B|$ is very close to zero at almost every point of the curve, and according to Eq.(5.5) the value of g_{TB} is expected to diverge.

Although for the calculation of g_{TB} shown in Figure 6.2 we have chosen the parameters $\alpha = 0$ and $\gamma = 0.5$, for the coming calculations of g_{TB} we do not need to find the precise coefficients α , γ that provide the most accurate description of the real density of states. Rather, we just adapt the width and height of the contour shown in Figure 6.2, to fit well the computational density of states, g_C , calculated using SIESTA.

In view of the new contour depicted by Figure 6.2, we can expect a different dependence than in the free electron case between the energy of the last occupied state relative to the ground state of the band, $\mu_{||}$, and the electron density n . In consequence, a different in-plane contribution is expected. To visualize the new scenario, in Figure 6.3 we compare the filling rate at g_{FE} (i.e. the DOS in the free electron case) and g_{TB} . Namely, the new $d\mu_{||}/dn$ will no longer be constant, as we expect a slowing down of $\mu_{||}$ at those densities corresponding to the half-full band, where the divergence is observed. Indeed, around the peak there are “infinitely many” states, and even though a new electron is added to the system there are yet other states available at very similar energies.

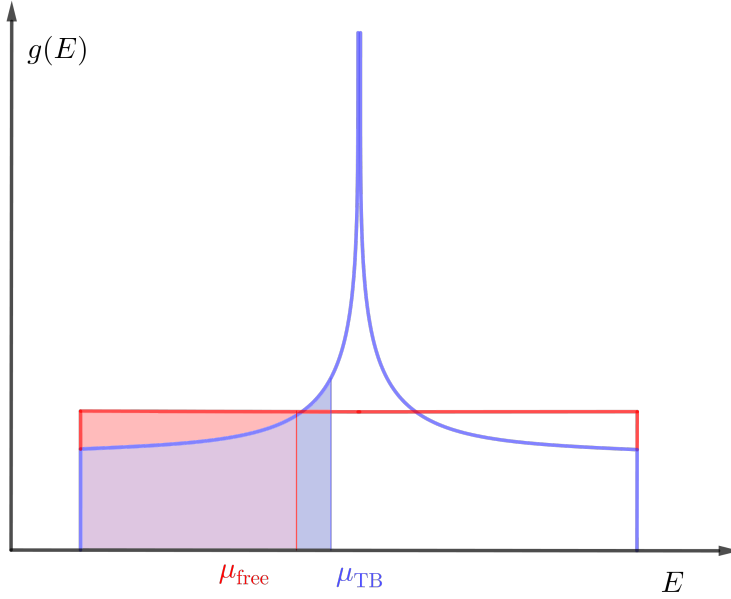


Figure 6.3: Comparison of the energies of the last occupied state, μ_{\parallel} , with respect to n , for the free electrons (red shape, μ_{free}) and tight-binding (blue shape, μ_{TB}) approximations. The electron density n is represented as the colored regions. Whereas the variation rate of μ_{free} with respect to n is linear (in Section Eq.3.1 we proved that $d\mu_{\text{free}}/dn = \pi/m_{\parallel}$), μ_{TB} is slowed down for those densities approaching the divergence.

6.2 Derivation of the in-plane contributions

In order to analyze our computational results, we shall first check whether the electronic structure at the 2D square quantum plate can be understood from a tight-binding perspective. In this case, it would be possible to test whether the electron compressibility $d\mu/dn$ of our quantum plate can be accurately computed using Eq.(4.1). Next, we justify that the tight-binding approximation is reasonable in our model.

In Figure 6.4, the first energy band of the 2D Na monolayer, computed using first-principle calculations (SIESTA), is shown. For the representation, we have chosen a lattice parameter of $a = 6.8\text{\AA}$. The plot depicts the exact shape that is expected for a tight-binding, meaning that this is certainly a good approximation for the real bonding of our system.

To gauge the similitude between the real electron bonding and the tight-binding approximation, we compare the density of states computed using first-principle calculations (again, SIESTA) and the corresponding calculations of g_{TB} , computed as explained in the previous section. In Figure 6.5, we represent the computational DOS g_{C} together with g_{TB} , for the lattice parameters of $a = 4.5\text{\AA}$, $a = 6.8\text{\AA}$ and $a = 7.5\text{\AA}$.

Among the three plots collected in Figure 6.5, only the one at $a = 6.8\text{\AA}$ has the same even parity as the g_{TB} . Despite the soft shape of the g_{C} , the g_{TB} can quantitatively approximate the g_{C} reasonably well, with the exception of the borders and obviously the divergence. On the other hand, the shape of the g_{C} is qualitatively closer to the g_{TB} at $a = 4.5\text{\AA}$, as the pronounced drop of the number of states at the borders coincides with the tight-binding case. Nevertheless, even though the divergence is also better reflected

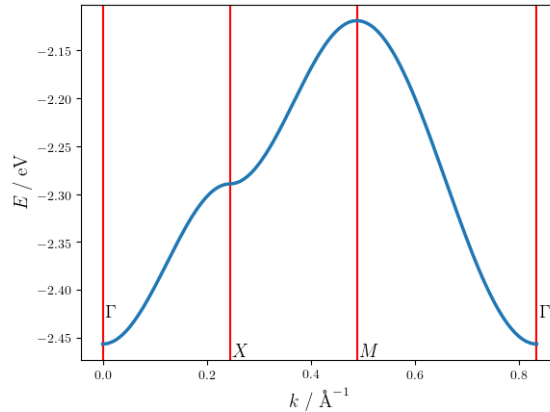


Figure 6.4: First energy band at the 2D square quantum plate, with $a = 6.8\text{\AA}$. The shape coincides the expected for a tight-binding, and thus the electron orbitals can be approximated within this approach.

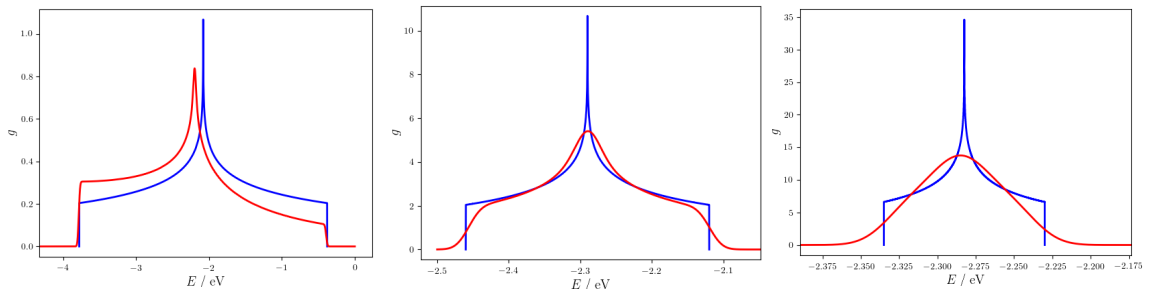


Figure 6.5: Comparison of the density of states at the quantum plate using first principle calculations (using the SIESTA code, blue line) and the tight-binding approach (red line).

From left to right, the images correspond to a lattice parameter of: 4.5\AA , 6.8\AA , 7.5\AA .

at $a = 4.5\text{\AA}$ (singular shape), g_C is no longer neither centered nor symmetrical. Furthermore, there are more states at lower energies, and fewer than the predicted within the tight-binding model for the greatest energies. The explanation is that, as the atoms of the lattice get closer, the overlapping of the orbitals increases. Hence, the tight-binding description with only nearest-neighbors interactions becomes insufficient. At $a = 4.5\text{\AA}$ the contribution of more distant atoms is not negligible, and breaks down the symmetry observed in our tight-binding model, where only the s orbitals are considered to set the energy band up. However, the g_{TB} is again a reasonable approximation for g_C , as it encompasses all the qualitative peculiarities of its contour. Regarding the $a = 7.5\text{\AA}$ graphic, there is not similarity neither qualitatively nor quantitatively between the g_C and the g_{TB} . At such a large distance, the overlapping between the atomic orbitals is negligible, and the g_C curve corresponds to the density of states of a 2D crystal with almost individual atomic orbitals. Indeed, the energy domain of this DOS is remarkably narrower than in the other two cases (almost all the states have energies between -2.36 eV and -2.24 eV).

Dismissing the $a = 7.5\text{\AA}$ case for not resembling the lattice bonding adequately, we compute the in-plane contributions for the $a = 4.5\text{\AA}$ and $a = 6.8\text{\AA}$ cases. For such purpose, we use two different inputs: the computational DOS (computed by SIESTA) g_C , and the

tight-binding DOS g_{TB} . In Figures 6.6-6.7 we include the curves of the energies of the last populated state with respect to the band ground state, μ_{\parallel} , and its derivative with respect to n , computed using first-principle calculations, for the $a = 4.5\text{\AA}$ and $a = 6.8\text{\AA}$ cases respectively. Together with these graphics, at the right column of each figure, we include the same magnitudes calculated from the tight-binding perspective.

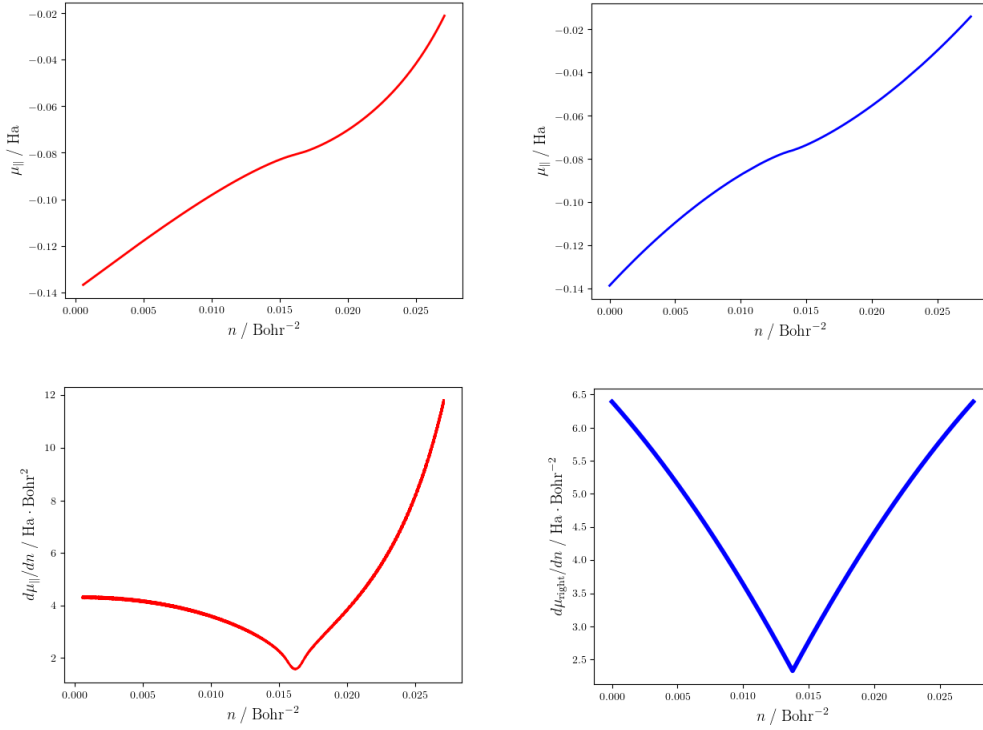


Figure 6.6: Left column: the upper graphic corresponds to the variation of μ_{\parallel} as a function of the electron density n , calculated from the computational density of states g_C . The lower plot depicts the first derivative of the upper curve with respect to the electron density, which coincides with the in-plane contribution. Right column: the same magnitudes, in the same order, computed from the tight-binding density of states g_{TB} . The calculations correspond to a lattice parameter of $a = 4.5\text{\AA}$.

6.3 Calculations for $a = 4.5\text{\AA}$

Up to this point we present our main results, starting with those for $a = 4.5\text{\AA}$. In this section, as well as in Section 6.4, the results are introduced in the following order: the electron compressibility $d\mu/dn$, the image charge center z_{im} , and the inverse capacitance density \mathcal{C}^{-1} .

In Figure 6.8, the curve of the electron compressibility, computed with using Eq.(5.8), is shown as a green curve. From now on, we shall refer to this as $(d\mu/dn)_{\text{num}}$ to emphasize that these values have been computed directly from the numerical differentiation of the Fermi levels μ that SIESTA outputs.

At first sight, in the low density regime the shape of the electron compressibility curve has the same qualitative form as all the examples studied in Section 3.2, corresponding to

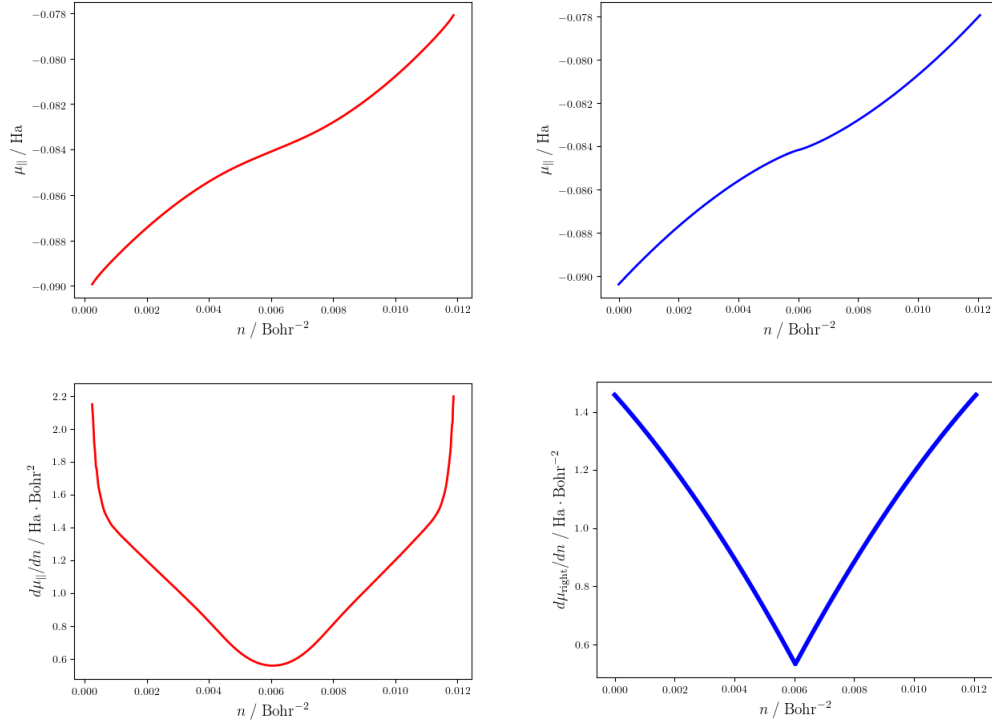


Figure 6.7: This figure represents exactly the same magnitudes as Figure 6.6, using the same structure, for a lattice parameter of $a = 6.8\text{\AA}$.

calculations of free electron models over finite wells and jellium slabs. Analogously to these free electron models, the evolution of the compressibility at the low n regime is determined by the variation of the exchange interactions along the z axis, i.e. Δ_{xc} . In particular, the behavior resembles that of the 2D free electron gas studied in the Section 3.2.1, for which we explained that $\Delta_{\text{xc}} \propto n^{1/2}$. In addition to this fact, the compressibility turns out to be negative for all the electron densities for which only the first energy band is populated. This is positive from the device manufacturing point of view, as it guarantees that the contribution of $d\mu/dn$ is to enhance the capacitance of the system. Hence, although physically implausible, the 2D monoatomic layer of Na might be an adequate structure for the construction of capacitor electrodes.

A remarkable difference with respect to the free electron models is the appearance of a pronounced drop at $n_{\text{D}} \sim 0.016 \text{ Bohr}^2$). This is a deviation from the models studied to this date, and does not have any precedents. As the only difference between our analysis and that carried out for free electron models is the in-plane contribution, this must be the cause of the anomaly.

We now focus on the other curves represented together with $(d\mu/dn)_{\text{num}}$ in Figure 6.8. The perturbation of the Hamiltonian along the z axis, computed as explained in Section 5.3.3 from Eqs.(5.11) and (5.11), is represented as a black line. In view of Figure 6.8, the perturbative term coincides with $(d\mu/dn)_{\text{num}}$ qualitatively, and almost quantitatively in the low density limit. Besides, we can assess that the perturbative term is not the cause of the anomaly observed in the contour of $(d\mu/dn)_{\text{num}}$, as at the densities where the drop occurs the shape of Δ_{tot} is uniform.

Recalling Eq.(4.1), the electron compressibility can be decomposed theoretically as

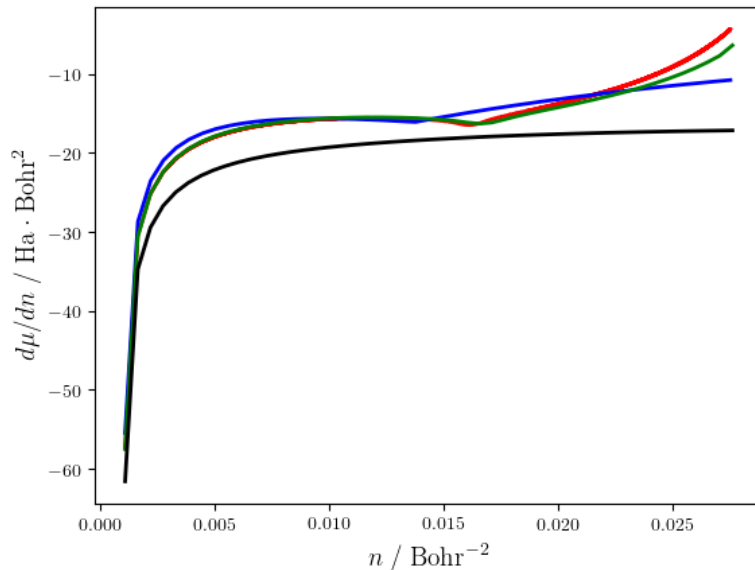


Figure 6.8: Electron compressibility of the quantum plate as a function of n , computed at $a = 4.5\text{\AA}$. The magnitudes represented are $(d\mu/dn)_{\text{num}}$ (green), $(d\mu/dn)_{\text{C}}$ (red) and $(d\mu/dn)_{\text{TB}}$ (blue), and the perturbation of the Hamiltonian Δ_{tot} (black). At the low n regime the contour of the curves is qualitatively the same as in the free electron case, showing a dramatic decline for low electron densities n . In this region, the contour of $(d\mu/dn)_{\text{C}}$ and $(d\mu/dn)_{\text{TB}}$ is dominated by the perturbative term. Albeit, this is no longer true for larger densities, as drop of the compressibility is observed at $n_{\text{D}} = 0.016 \text{ Bohr}^2$. The matching between $(d\mu/dn)_{\text{num}}$ and $(d\mu/dn)_{\text{C}}$ is excellent. On the other hand, although $(d\mu/dn)_{\text{TB}}$ depicts the same qualitative behavior as $(d\mu/dn)_{\text{num}}$, the values are slightly different and the drop is predicted at lower densities.

the sum of the perturbation Δ_{tot} and the in-plane contribution $d\mu_{\parallel}/dn$. This equation provides an accurate quantitative description of the electron compressibility for the free electron models studied in [JGFS19]. We are interested in testing whether is it yet valid to the extent of the 2D square monoatomic layer of Na that we are working with. From the observation of Figure 6.8, and as explained in the previous paragraph, we already know that the major contribution to the compressibility arises from the perturbation with respect to n of the Hamiltonian along the z axis. Nevertheless, we would like to find out whether the difference between the $(d\mu/dn)_{\text{num}}$ (green) and the Δ_{tot} (black) curves coincides with the in-plane contribution of the density of states. For such purpose, we shall compute the in-plane contribution in two different ways: using the computational density of states g_{C} obtained from the first-principle calculations of SIESTA, and using the tight-binding density of states g_{TB} , deduced as explained in Section 6.1. The in-plane contributions for these two approaches have already been computed in Figure 6.6.

The red and blue curves represented in Figure 4.1 correspond to the theoretical electron compressibilities computed, respectively, using the computational and the tight-binding in-plane contributions in Eq.(4.1). According to the notation for $(d\mu/dn)_{\text{num}}$, we refer to each of the new compressibilities as $(d\mu/dn)_{\text{C}}$ (computed using the SIESTA density of states, g_{C}), and $(d\mu/dn)_{\text{TB}}$, (computed using the tight-binding density of states, g_{TB}).

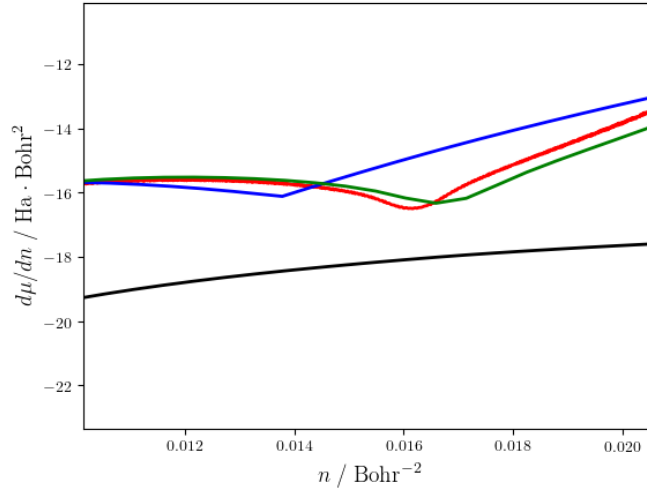


Figure 6.9: Enlarged vision of Figure 4.1 around the anomaly of the compressibility.

It stands out the excellent agreement between the values of $(d\mu/dn)_{\text{num}}$ and $(d\mu/dn)_{\text{C}}$. Indeed, both curves are practically indistinguishable for almost all the range of densities studied. Nevertheless, the theoretical prediction of $(d\mu/dn)_{\text{C}}$ provides values that are slightly above our numerical calculations for densities greater than $n = 0.029 \text{ Bohr}^{-2}$. Regarding the $(d\mu/dn)_{\text{TB}}$ curve, it provides a good qualitative description of the electron compressibility, but the numerical difference with respect to $(d\mu/dn)_{\text{num}}$ is larger. Namely, the $(d\mu/dn)_{\text{TB}}$ curve predicts that the drop in the compressibility is slightly displaced with respect to the $(d\mu/dn)_{\text{num}}$ case.

In view of the results, we can assess that the anomaly in the contour of the density of states is caused by the in-plane contribution. Indeed, we have justified that it cannot be due to the perturbation Δ_{tot} , and there are only two contributions to the compressibility according to Eq.(4.1). In addition to this fact, in the neighborhood of the drop the compressibility depicts the same shape as the in-plane contributions gathered in Figure 6.6. The origin of the rupture with the uniform shape of the compressibility characteristic from the free electron models, is the appearance of a peak in the density of states. As we can observe in Figure 6.6, the variation of μ_{\parallel} with respect to n is not linear as in the free electron case. When the electrons start the band filling (i.e. at $n \sim 0$), the variation of μ_{\parallel} is locally linear and the behavior is the same as in the free electron case. Hence, the local in-plane contribution $d\mu_{\parallel}/dn$ is approximately constant. However, this trend is stopped as the electrons approach the states that constitute the peak of the DOS. Thus, the variation of μ_{\parallel} is progressively slowed down until the peak is achieved. Later on, as more electrons fill the band, the opposite trend is observed and μ_{\parallel} accelerates until the completion of the band. Therefore, the presence of the peak at the density of states is the cause for the appearance of the drop in the electron compressibility.

According to the explanation of the previous paragraph, it is immediate to understand why the drop of $(d\mu/dn)_{\text{TB}}$ is displaced with respect to the other compressibilities. Recalling Figure 6.5, the position of the peak at g_{C} and g_{TB} is different. Hence, the predicted drops must also occur at different densities.

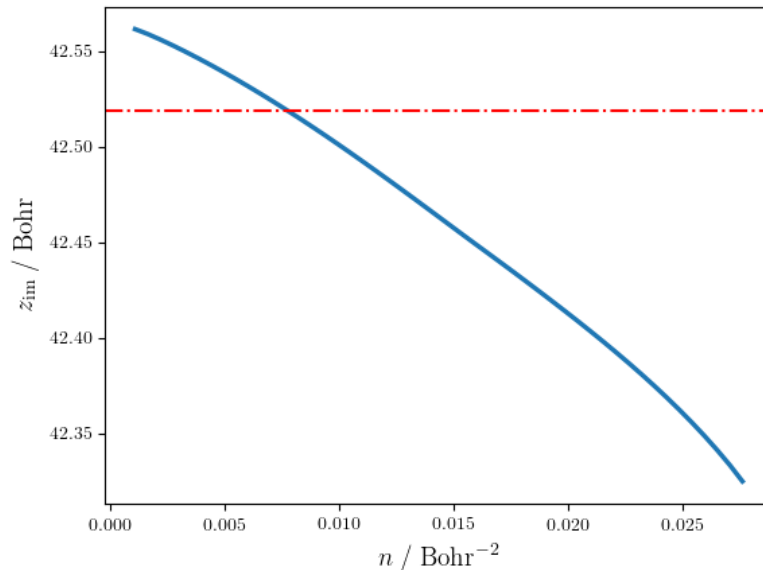


Figure 6.10: Image charge center z_{im} as a function of the electron density n , computed for a lattice parameter of $a = 4.5\text{\AA}$. The position of the quantum plate $z = d$ is drawn as a horizontal, dashed line. Remarkably, for the lowest values of n the image charge center moves away from the classical electrode. Albeit, z_{im} progressively approaches the front plate as n increases, in an approximately linear way.

To better gauge the accuracy of the theoretical description of the electron compressibility given by Eq.(4.1), in Figure 6.9 we show an expanded vision of the same curves plotted in Figure 6.8 in the neighborhood of the drop. The image illustrates that the matching between $(d\mu/dn)_{\text{num}}$ and $(d\mu/dn)_{\text{C}}$ is not perfect in the closeness of the drop, as both curves predict a slightly different position for this one. Albeit, the difference between the predicted density is lower than $\delta n = 0.001$, and the agreement is yet very good. As we have already pointed out, the electron density for which the drop is predicted by $(d\mu/dn)_{\text{TB}}$ is not precise.

We now proceed to analyze the variation of the image charge center, z_{im} , with respect to n . In Figure 6.10, z_{im} is plotted as a function of the electron density. To better envision the effect of electron confinement, and to compare the displacement of z_{im} with respect to the position of the quantum plate in the z axis, we draw an horizontal dashed line representing the quantum plate location, $z = d$.

As we expected from the analysis of the free electron models, the image charge center approaches the classical electrode as n increases. Indeed, the electrons feel the attraction of the extra charge that accumulates on the front plate. The observed contour is qualitatively the same as the one shown in Figure 3.5, corresponding to the square quantum wells containing a free electron gas. However, our curve depicts a rupture of the linearity for the lowest and greatest densities.

Regarding the impact of the z_{im} contribution on the capacitance, as $z_{\text{im}} < d$ for all the densities greater than $n = 0.008 \text{ Bohr}^{-2}$, the contribution to the inverse capacitance density will be an approximately linear decrease. However, for densities below $n = 0.008 \text{ Bohr}^{-2}$, the effective interplate distance is larger than in the classical case.

Thus, the total capacitance is hence affected negatively. In spite of this fact, the divergence caused by the electron compressibility at $n = 0$ vastly overcompensates the image charge effect, and the overall capacitance is yet enhanced.

A possible explanation for the distancing observed at the low n regime is the fact that, at these small densities, in the quantum electrode there is yet an excess of protons over the number of electrons. Thus, as the overall capacitor must remain neutral, the classical electrode must conversely host an excess of electrons. According to this, the few electrons at the quantum plate feel the repulsion of those at the front plate and hence accumulate further, leading to an enlargement of the virtual interplate distance.

After having analyzed the electron compressibility and the image charge center contribution, we can assess that the quantum capacitance of our system is larger than its classical analogue. Indeed, we have seen the contribution of z_{im} is better than its classical analogue for sufficiently large n , and in the low density limit the electron compressibility, which is always negative, diverges towards negative values. In Figure 6.11, the inverse capacitance density \mathcal{C}^{-1} , computed as the sum of the electron compressibility $(d\mu/dn)_{\text{num}}$ and the image charge center contribution $4\pi z_{\text{im}}$, according to Eq.(3.2), is represented as a function of n .

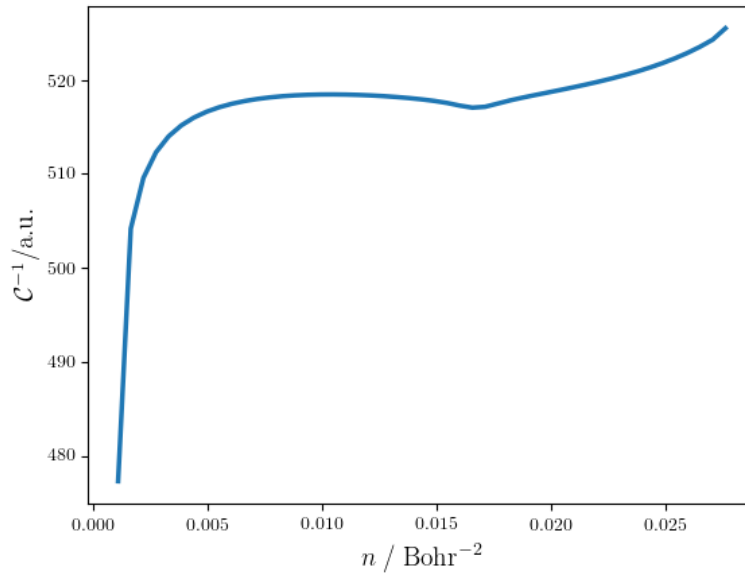


Figure 6.11: Inverse capacitance density \mathcal{C}^{-1} (a.u.) of the capacitor model presented in 4.2, for a lattice parameter of $a = 4.5\text{\AA}$, computed as the sum of the electron compressibility $(d\mu/dn)_{\text{num}}$ and $4\pi z_{\text{im}}$, according to Eq.(3.2).

Although the dominant contribution is the “classical” term $4\pi z_{\text{im}}$, which leads to the observed positive values, the contour of the curve is determined by the electron compressibility. As in the case of the electron compressibility, the curve coincides qualitatively with the inverse capacitance densities gathered in Figure 3.4, corresponding to the free electron gasses enclosed within square quantum wells. However, the presence of the drop at $n_{\text{D}} \sim 0.016 \text{ Bohr}^{-2}$ is not reflected in free electron models, as it is caused by the non-constant in-plane contribution.

6.4 Calculations for $a = 6.8\text{\AA}$

In the present section, we include our results for $a = 6.8\text{\AA}$. We follow the exact structure and notation as in Section 6.3. In Figure 6.12, the curve of the electron compressibility computed from Eq.(5.8), $(d\mu/dn)_{\text{num}}$ is shown in green.

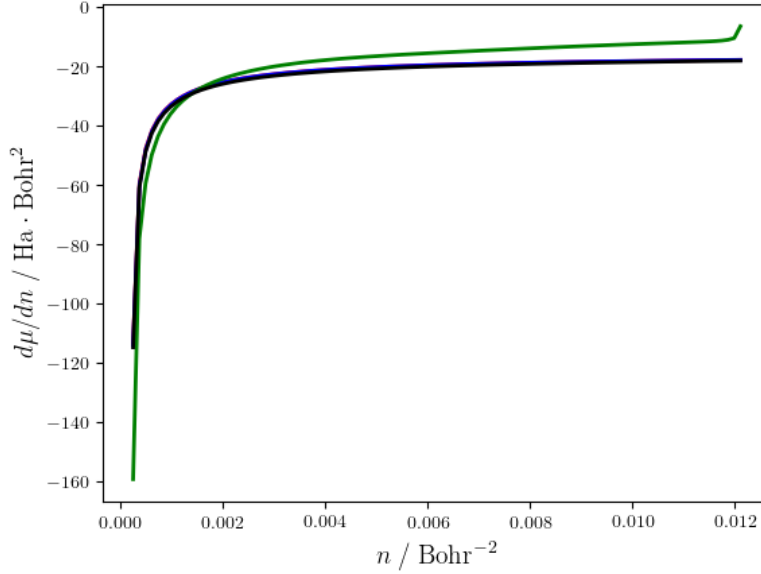


Figure 6.12: Electron compressibility of the quantum plate as a function of n , computed at $a = 6.8\text{\AA}$. The magnitudes represented are $(d\mu/dn)_{\text{num}}$ (green), $(d\mu/dn)_C$ (red) and $(d\mu/dn)_{\text{TB}}$ (blue), and the perturbation of the Hamiltonian Δ_{tot} (black). In contrast to the $a = 4.5\text{\AA}$ case, the contour of all the curves is homogeneous and no drop is observed.

Besides, the perturbative term Δ_{tot} practically coincides with the theoretical compressibilities $(d\mu/dn)_C$ and $(d\mu/dn)_{\text{TB}}$, and there is not an accurate agreement between the Eq.(4.1) and our numerical calculations of $(d\mu/dn)_{\text{num}}$.

A qualitatively relevant discrepancy with respect to the contour of the compressibility computed at $a = 4.5\text{\AA}$ (Figure 6.8) is observed, as the drop detailed in the previous section is no longer present. Indeed, the new contour of $(d\mu/dn)_{\text{num}}$ resembles much more to the compressibilities of the free electrons represented as dashed lines in Figure 3.4. As from the study of the $a = 4.5\text{\AA}$ we found that the drop was produced by the in-plane contribution, we might infer that the in-plane contribution is negligible at $a = 6.8\text{\AA}$.

Regarding the perturbative term Δ_{tot} , represented in black, it again differs from the $a = 4.5\text{\AA}$ case. Even though its shape is qualitatively the same as that corresponding to free electron models and the one obtained at $a = 4.5\text{\AA}$, it overcomes the $(d\mu/dn)_{\text{num}}$ curve for densities below $n = 0.0018 \text{ Bohr}^{-2}$. This phenomena makes impossible the agreement between the theoretical compressibility, computed from Eq.(4.1), and the numerical value of $(d\mu/dn)_{\text{num}}$. The reason is that, for both the theoretical and numerical magnitudes to coincide, it would be necessary that the in-plane contribution $d\mu_{\parallel}/dn$ returned negative values. This would imply the fact that, as more electrons populate the band, the energy of the last occupied state relative to the ground state of the band should decrease, something absurd. Hence we cannot guarantee that the decomposition of Eq.(4.1) is yet valid for the

case of $a = 6.8\text{\AA}$.

To complete our study of the electron compressibility, we focus on the theoretical calculations of $(d\mu/dn)_C$ (represented in red) and $(d\mu/dn)_{TB}$ (in blue), computed using Eq.(4.1). In this case, in-plane contributions collected in Figure 6.7 are used. Remarkably, the in-plane contributions are to all effects negligible with respect to the perturbation Δ_{tot} , and the curves corresponding to Δ_{tot} , $(d\mu/dn)_C$ and $(d\mu/dn)_{TB}$ virtually coincide. Namely, the $(d\mu/dn)_C$ and $(d\mu/dn)_{TB}$ curves are entirely covered by Δ_{tot} , and cannot be distinguished in Figure 6.12. In particular, as we expected from the observations made in the previous paragraph, there is not agreement between $(d\mu/dn)_{num}$ and Eq.(4.1).

We continue with the z_{im} results. Figure 6.13 depicts the variation of the image charge center z_{im} as a function of n . The evolution of z_{im} does not exhibit any relevant discrepancy with that one computed for $a = 4.5\text{\AA}$ in Figure 6.10. Again, the image charge center approaches the front plate as the electron density of the quantum plate (and hence, the attraction of the classical electrode) increases. In consequence, the effect is to reduce the inverse capacitance density of the system, or equivalently, to enhance the total capacitance of the system. The unique interesting comment to do is the fact that the approach of z_{im} to the classical plate is softened for the largest values of the capacitance. This effect is due to the electron confinement at the quantum plate: the resistance of electrons to leave the plate. This exact behavior is observed in the z_{im} curves of Figure 3.5, as the electron confinement is well represented by the finite, square wells. The reason why this is not observed for the $a = 4.5\text{\AA}$ case is that, for the latter, the electrostatic attraction between the plates is sensibly larger (the Coulomb potential decays $\propto r^{-2}$).

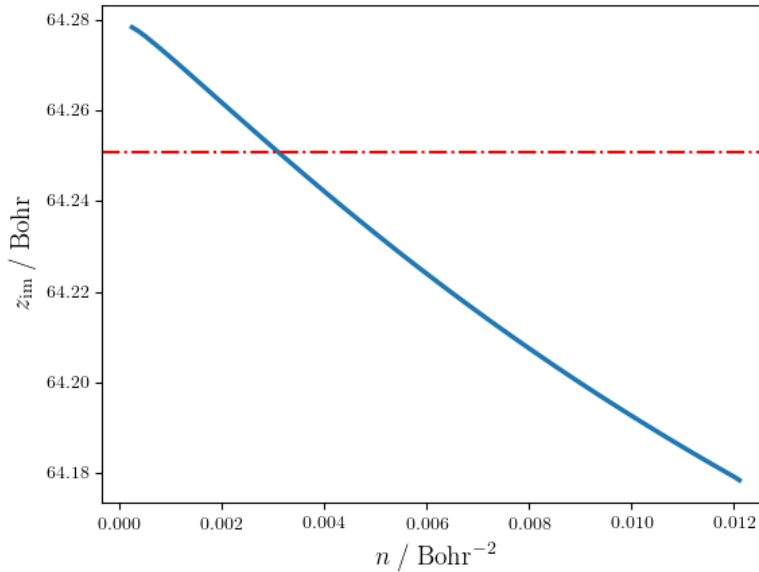


Figure 6.13: Variation of the image charge plane position z_{im} with respect to n , at $a = 6.8\text{\AA}$. To better envision the displacement of the electron cloud, the position of the geometric center of the quantum plate has been drawn as a red dashed line.

To conclude this Chapter, in Figure 6.14 we present the inverse capacitance density \mathcal{C}^{-1} of our capacitor model, for $a = 6.8\text{\AA}$. Surprisingly, the curve is qualitatively closer to the inverse capacitance of the free electron gases contained within finite, square wells

(presented in Figure 3.4) than to the equivalent curve for computed for $a = 4.5\text{\AA}$. Indeed, no drop or anomaly in the $(d\mu/dn)_{\text{num}}$ curve was observed, and the electron confinement at $a = 6.8\text{\AA}$ is similar to that attached to the finite wells. The variation in the scale of the inverse capacitance with respect to Figure 6.11 is due to the plate separation. In our simulations, the separation between the the plates was chosen to be proportional to the lattice parameter. Hence, the obtained capacitances for $a = 4.5\text{\AA}$ must necessarily be larger than those calculated for $a = 6.8\text{\AA}$.

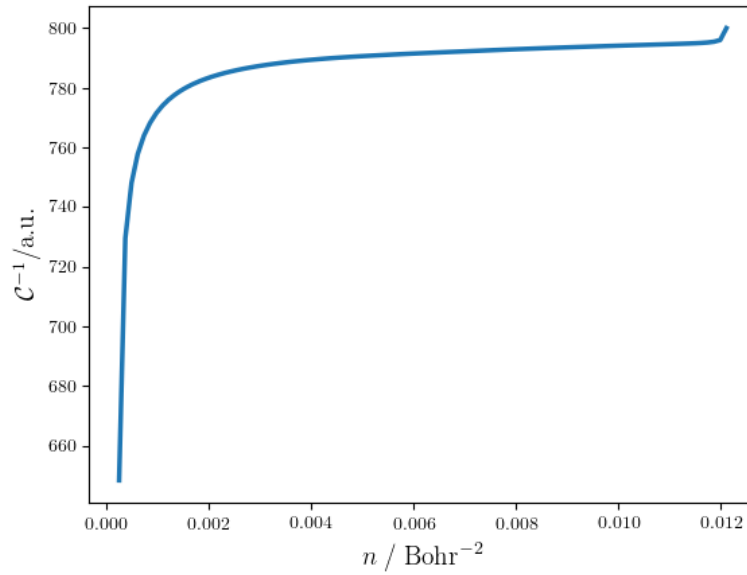


Figure 6.14: Inverse capacitance density C^{-1} (a.u.) of the capacitor model presented in 4.2, for a lattice parameter of $a = 6.8\text{\AA}$, computed as the sum of the electron compressibility $(d\mu/dn)_{\text{num}}$ and $4\pi z_{\text{im}}$, according to Eq.(3.2). The contour of the curve resembles the calculations for free electron gases contained in finite, square quantum wells shown in Figure 3.4, and no drop is observed as in the $a = 4.5\text{\AA}$ case.

Chapter 7

Discussion

One of the most remarkable issues derived from our results is the fact that, even though the Eq.(4.1) provided an accurate description of the capacitance at $a = 4.5\text{\AA}$, it does not work well at $a = 6.8\text{\AA}$. Indeed, the in-plane contributions computed for this lattice parameter is negligible in comparison to the perturbation Δ_{tot} , and insufficient to account for the separation of the curves. To understand this phenomenon, it is convenient to take a step back to the justification of the tight-binding approximation. As we have explained in Chapter 4, the energy dispersion relationship of Eq.(5.3) only takes into account the interaction of s orbitals with exclusively the first neighbors. Recalling Section 5.2, we used s orbitals in our base of localized atomic orbitals, meaning that the first of the last two assumptions is well reflected in our calculations. Albeit, in order to guarantee that there were not overlapping between the orbitals of more distant neighbors, we chose a relatively large lattice parameter of $a = 6.8\text{\AA}$ for our calculations. The shape of the bands, shown in Figure 6.4, as well as density of states of Figure 6.5 guaranteed that, indeed, the electrons inside the quantum plate can be well approximated using from the tight-binding perspective. Despite this fact, the separation of $a = 6.8\text{\AA}$ is large enough to constrain all the states in a very small interval of energies. Namely, in view of Figure 6.5, at $a = 6.8\text{\AA}$ all the states of the band have energies between -2.5 and -2.1 eV. This range of energies is very narrow, and in particular, it implies that the variation of the energy of the last occupied state with respect to n , $d\mu_{\parallel}/dn$, cannot be large. Hence, the insufficiency of Eq.(4.1) for describing the electron compressibility at $a = 6.8\text{\AA}$ must be a consequence of low energy dispersion of the electronic states that constitute the band. The orbital overlapping at $a = 6.8\text{\AA}$ is so small that electron states do not have to broaden their energies very much, leading to quasi-atomic energies.

The results included in Section 6.3 have demonstrated that the decomposition of the electron compressibility provided by Eq.(4.1) is completely valid in our model, at $a = 4.5\text{\AA}$. This equation, firstly deduced and employed in [JGFS19] for the study of free-electron-like electrodes, has resulted to be valid to the extent of plates modelled as 2D square, monoatomic lattices of Na. Indeed, we have computed the electron compressibility following completely different procedures. For the calculation of $(d\mu/dn)_{\text{num}}$, we have used Eq.(5.8) and the Fermi levels returned by SIESTA. Conversely, for $(d\mu/dn)_{\text{C}}$ we have computed the perturbation Δ_{tot} as explained in Section 5.3.3, from the map of the Hartree and exchange-correlation potentials along the z direction, $V_{\text{H}}(z)$ and $V_{\text{xc}}(z)$ respectively. In addition to this, we had to derive the in-plane contribution $d\mu_{\parallel}/dn$ for the computational density of states g_{C} that SIESTA outputs. Even though these two procedures are completely independent, they have produced very similar

results. The fine discrepancies observed in the enlarged vision of Figure 6.9 can be understood within the numerical uncertainty introduced by the methods employed for the calculations. In particular, a possible cause for the small discrepancies might be the numerical differentiation. This method is strongly reliant on the number of points of the n sampling, especially at those regions where rapid variations of curve occur. The major discrepancies are observed at the closest densities to the drop observed in Figure 6.8, where the derivative of the compressibility is momentarily zero. Thus, this might entail a small error in either the calculation of the in-plane contribution or the numerical derivation of the Fermi level. Besides, only 50 points in the n sampling were used to draw this curve, and very likely a larger sample would provide a better agreement between the curves.

Regarding the calculation of the in-plane contribution, we have carried out a simplification that, although in view of the results shown in Figure 6.8 does not have a great impact, we point out here. The curves shown in Figures 6.6 and 6.7, corresponding to the in-plane contributions computed from the computational and the tight-binding density of states respectively, have been calculated for the neutral system, i.e. for an electron density at the quantum electrode of $n_{\text{HF}} = 1/a^2$ (where the band is half-filled). This entails the assumption that the contour of the density of states does not vary as the electron density n increases. Unfortunately, this is not necessarily true. Even though our calculations of $(d\mu/dn)_{\text{C}}$ have turned out to provide an accurate description of $(d\mu/dn)_{\text{num}}$, another possible cause for the remaining separation between the theoretical and numerical electron compressibility might also be this simplification. In future works, we aim to include this insufficiency as part of our code, to achieve a complete matching between the theoretical and numerical compressibility curves.

For the first time, in this work the curves of the inverse capacitance densities \mathcal{C}^{-1} have been calculated for electrodes that include the atomic nature of matter. As mentioned in the Introduction, the motivation for this work was double. Firstly, we wanted to check whether the conclusions derived from the free electron models studied in [JGFS19] were yet valid for a simple atomic model such as the 2D square, monoatomic layer. However, and more importantly than the first milestone, this work pursued the disclosure of new agents contributing to capacitance, introduced by the discretization of matter. For this reason, one of the successes of this work is the observation of the drop in the \mathcal{C}^{-1} curve, introduced by the variation in the contour of the density of states. The presence of the drop is beneficial, as it leads to a capacitance enhance. More specifically, the in-plane term pushes $d\mu/dn$ towards negative values, even for densities outside the low n regime where the divergence occurs (this is, for instance, the case of $a = 4.5\text{\AA}$). In vision of our results, we can conjecture a new possible path for further enhancing the capacitance, based on the in-plane contribution. According to Eq.(5.7), the qualitative shape of the in-plane contribution $d\mu_{\parallel}/dn$ coincides with that of the inverse density of states, $1/g$. As in our case the DOS showed a peak, a drop was observed in the compressibility. Therefore, the in-plane contribution can be directly modelled from the density of states. If we are interested in the construction of capacitors with a large capacitance improvement at a certain density n , we shall look for structures where the energy of the last occupied state, $\mu_{\parallel}(n)$, lies in a region of the band with many available states, i.e. where g is large. Besides we can guarantee that, to the extent where Eq.(4.1) is yet valid, the in-plane contribution will only be constant if g is also constant, i.e. if the system is a 2D free electron gas. In order to study the possibilities and the accuracy of the assertions of this paragraph, more investigation is required in other structures than 2D square lattices.

This work is a good first step towards further research in the effect that atomic electrodes exert on the total capacitance of a system. Indeed, the software here developed can be used to repeat exactly the same calculations for systems with other structures. For instance, the structure of the quantum plate of Figure 4.3 can be replaced by a 2D graphene-like monolayer, a monoatomic cubic layer, or a multiatomic 2D layer. Nevertheless, the understanding of these systems from a theoretical point of view can be notably more complex, and revisiting the theory that backs up our calculations shall become necessary. The reason for choosing the Na-monolayer is that it is the simplest atomic model. We have succeeded in the verification that the decomposition of $d\mu/dn$ of Eq.(4.1) is valid to the extent of our model, but more research is required in order to test its validity for some of the other structures mentioned in this paragraph.

Chapter 8

Conclusions

Based on the free electron models studied in [JGFS19], we have designed a parallel-plate capacitor that enables to study the contribution of an electrode, modelled as a 2D square monoatomic layer of Na, to the total capacitance of the system. For our calculations, we have taken advantage of the theoretical construction of [JGFS19]. Albeit, we had to generalize the contribution of the in-plane density of states to the case of a plane of atoms in a square lattice with one s -orbital per site.

We have computed the electrode contributions to the inverse capacitance of our system at the quantum level: the electron compressibility and the image charge geometrical capacitance. The electron compressibility has been calculated in three different ways. Firstly, it has been derived numerically from first-principle calculations on the Fermi level of the quantum plate of our capacitor model. Secondly, we have computed the sum of the perturbative terms due to the variation of the Hartree and exchange-correlation potentials along the z direction, as well as the in-plane contribution coming from the population of the density of states. For such purpose, we have computed the density of states within two different approaches, a first-principle calculation based on the software SIESTA and the tight-binding model. Regarding the image charge contribution, we have tracked the variation of the image charge center as n changes. Our results have been reproduced for the lattice parameters of $a = 4.5\text{\AA}$ and $a = 6.8\text{\AA}$ of the square lattice.

For the case of $a = 4.5\text{\AA}$, the numerical results of the compressibility have turned out to be in complete agreement with those computed from Eq.(4.1), using the first-principle density of states. This implies that theoretical decomposition deduced in [JGFS19] for simple free electron and jellium models is yet valid to the extent of our 2D lattice. The computed electron compressibility and the image charge contributions have demonstrated that the behavior of the capacitance in our model is to all effects equivalent to that of a free electron system in the low electron density regime. Nevertheless, the deformation of the density of states attached to our lattice has led to the formation of a drop in the inverse capacitance curve. This phenomenon, with no precedent within free electron models, results on a further enhance of the capacitance. Regarding our calculations on the tight binding model, even though the results do not accurately coincide with the numerical results, the qualitative shape of the electron compressibility is well described.

The same conclusions are not shared at the $a = 6.8\text{\AA}$ case, as the theoretical and numerical electron compressibilities do not match well. The reason is that the formed energy band is very narrow, and the dispersion of the energy levels is quasi-atomic. At $a = 6.8\text{\AA}$, the agreement with free electron models confined in square wells is remarkable, and no drop is observed in the contour of the inverse capacitance.

In view of the results, we can ensure that most of the conclusions derived from free electron models are valid to the extent of square monoatomic layers. However, new effects must be taken into account when dealing with atomic electrodes, as the shape of the density of states is directly related to the in-plane contribution. Nevertheless, as in our $a = 4.5\text{\AA}$ case, the variations with respect to the free electron models can be positive in the sense that they can lead to enhances of the capacitance. A long track of research is yet required to ensure whether or not the theoretical decomposition of the in-plane contribution used in this work is yet valid for more complex structures. The present work is a good starting point for further investigation, and we have developed the software for the analysis of more complex structures, that we shall study in the near future.

Chapter 9

Appendix: the Python code

For the obtaining of the results collected in Chapter 6, a large number of calculations were required. In particular, the interplay between SIESTA and our own code has been a key point for the computation of all the relevant magnitudes exposed in Chapter 5. Because of the importance of the code in this work, and as we target to further employ and debug it for more complex calculation, we devote this appendix to a global of our software. We split our programs in 3 groups: the master program, the calculations on the density of states, and the graphical representation of the magnitudes of interest.

Name of the program	Description
electron_density.py	This is the main program for this work. As input, it receives parameters specified by the user to carry out the simulation. These parameters are: the folder where the SIESTA files necessary for the simulation are allocated and where the user desires to store the results file, the atomic number of the chosen species, the first and last lattice parameters for which the code has to run, the number of steps in the lattice parameter map, the lowest and greatest charge differences between the classical and the quantum plates, and the number of steps for the charge difference map (which is equivalent to a map over the electron density n). Internally, the code calls to SIESTA (and to its extension MACROAVE) to output the Coulomb potential V_H , exchange-correlation potential V_{xc} , total Fermi level μ , density of states g_C , and electron density function ρ for each (a_i, n_j) pair. The code stores all the outputs and saves the magnitude of interest in a text file, which in addition contains the numerical calculations independent from SIESTA explained in Chapter 5. Finally, the code outputs a text file containing tables of all the magnitudes of interest.

Table 9.1: Description of the master program of this work. This program has multiple methods. However, most of them very technical and do not provide any additional information to the description above.

Name	Description
DOS_calculations.py	This is a collection of methods for the calculation of the density of states within the tight-binding approximation, and for the derivation of the in-plane contributions.
Method	Description
par_plot	Computes and represents the equienergetic curves contained in the Brillouin zone, according to the band description of Eq.(5.3).
int_interes	Solves numerically the integral over one fourth of the equienergetic curve.
integral_definitiva	Computes the final density of states within the tight-binding approach for a given energy E .
normaliza_DOS	Generates the density of states computed within the tight-binding approximation normalized for a certain electron density n , with the borders at the energies given as input.
dmudn_comp	Reads the SIESTA output file of the density of states, and computes the corresponding variation of the energy of the last occupied state with respect to the electron density n . (i.e. this program computes the in-plane contribution using g_C)
dmudn_tb	Receiving the density of states computed within the tight-binding approximation as input, calculates the variation of the energy of the last occupied with respect to the electron density n .(i.e. this program computes the in-plane contribution using g_{TB})

Table 9.2: Description of the methods of the density of states group.

Name	Description
graficas.py	This is a collection of methods for the reading of the data of interest from the output text file of electron_density.py and its graphical representation
Methods	Description
lectura_inv_C	Reads the columns of the output text file that corresponds to the electron density n and the inverse capacitance density C^{-1} .
plot_inv_C	Represents graphically the data read by lectura_inv_C .
lectura_dmudn	Reads the columns of the output text file that corresponds to the electron density n and the numerical calculation of the electron compressibility $d\mu/dn$. Besides, it reads the variations of the last occupied state of the band $d\mu_{ }/dn$ stored in a different text file.
plot_dmudn	Represents graphically the data read by lectura_dmudn .
lectura_delta	Reads the columns of the output text file that corresponds to the electron density n and the perturbation of the Hamiltonian Δ_{tot} .
plot_delta	Represents graphically the data read by lectura_delta .
lectura_zim	Reads the columns of the output text file that corresponds to the electron density n and the image charge center z_{im} .
plot_zim	Represents graphically the data read by lectura_zim .
lectura_bands	Reads the SIESTA output file that stores the energy of the bands as a function of the wavevector.
plot_bands	Represents graphically the data read by lectura_bands .
lectura_DOS	Reads the SIESTA output file that stores the computational DOS, as well as the text file that contains the DOS computed within the TB approach.
plot_DOS	Represents graphically the data read by lectura_DOS .
comparative_dmudn	Represents in a single graphic the numerical and the theoretical values of the electron compressibility $d\mu/dn$.
test_masa_efectiva	Using the SIESTA output file that stores the band information, it realizes a parabolic fit at the ground state of the band, and returns the effective mass.

Table 9.3: Description of the methods in the graphical representation group.

Bibliography

- [FSL63] R. P. Feynman, M. Sands, and R. B. Leighton. *The Feynman Lectures on Physics. Volume 1*. California Institute of Technology, 1963.
- [JGFS19] J. Junquera, P. García-Fernández, and M. Stengel. Mechanisms to enhance the capacitance beyond the classical limits in capacitors with free-electron-like electrodes. *Physical Review B*, 99(235127), 2019.
- [KM09] T. Kopp and J. Mannhart. Calculation of the capacitances of conductors: Perspectives for the optimization of electronic devices. *Journal of Applied Physics*, 106(064504), 2009.
- [Moo98] G. E. Moore. Cramming more components onto integrated circuits. *Proceedings of the IEEE*, 86(1), 1998.
- [SAG⁺02] J. M. Soler, E. Artacho, J. D. Gale, A. García, J. Junquera, P. Ordejón, and D. Sánchez-Portal. The SIESTA method for *ab initio* order- N materials simulation. *Journal of Physics: Condensed Matter*, 14(11), 2002.
- [SD08] S. Salahuddin and S. Datta. Use of negative capacitance to provide voltage amplification for low power nanoscale devices. *Nano letters*, 8(2), 2008.
- [ZWH⁺16] P. Zubko, J. C. Wojdeł, M. Hadjimichael, S. Fernandez-Pena, A. Sené, I. Luk'yanchuk, J. Triscone, and J. Íñiguez. Negative capacitance in multidomain ferroelectric superlattices. *Nature*, 534(7608), 2016.